CRASHWORTHINESS ENERGY ABSORPTION OF CARBON FIBER COMPOSITES: EXPERIMENT AND SIMULATION

Francesco Deleo, Paolo Feraboli

University of Washington, Seattle, WA 98195-2400

Abstract

The higher mechanical characteristics and mass specific energy absorption capabilities of composite materials motivate their use in large primary structures as well as structural and crashworthy components over more traditional metallic designs. Numerical simulation has become a common tool in structural design and crashworthiness. A well-established simulation practice is needed to significantly reduce the amount of experimental testing required during product development and certification. Due to the complex mechanical behavior of advanced composite materials, the capability of the existing analytical and numerical models to predict the crushing behavior is limited. The merits and weaknesses of a progressive failure material model, MAT54, of a commercially available explicit finite element solver, LS-DYNA, are highlighted through single-element investigations. Then, the suitability of MAT54 to simulate the quasi-static crushing of a composite specimen is evaluated. Through extensive calibration by trial and error, the crushing behavior of a semi-circular sinusoid specimen comprised of carbon fiber/ epoxy unidirectional prepreg tape is properly simulated, both in terms of the specific energy absorption and load – penetration behavior. The study is extended to five different geometries in order to evaluate the effect of geometric features on crush behavior, both from an experimental and numerical standpoint. Finally an energy-absorbing composite sandwich structural concept, comprised of a deep honeycomb core with carbon fiber/ epoxy facesheets, subject to through-thickness crushing and penetration, is considered. With the aid of the building block approach and extensive calibration of the material models and contact formulations, the full-scale crush behavior is predicted.

Background and Requirements

Because of their higher mechanical properties to weight ratio, new generation supercars make use composite materials in primary structures in order to achieve better acceleration performance, better handling and dynamics. As less expensive manufacturing processes have been successfully implemented into production and fuel efficiency is becoming a more and more important design driving factor, composite materials are becoming an appealing alternative to traditional metallic designs into larger volume production automobiles. It has also been proved that, if properly designed, composite members can provide normalized energy absorption capabilities which are superior to those of metals, therefore making them an attractive choice of material for energy-absorbing structural devices [1].

The energy-absorption behavior of composites is not easily predicted due to the complexity of the failure mechanisms that can occur within the material. Composite structures fail through a combination of fracture mechanisms, which involve fiber fracture, matrix cracking, fiber-matrix debonding, and delamination [1]. The brittle failure modes of many polymeric composite materials can make the design of energy-absorbing crushable structures difficult. Furthermore, the overall response is highly dependent on a number of parameters, including the geometry of the structure, material system, lay-up, and impact velocity. Tubular structures are used by the

motorsport and automotive industries as dedicated members to absorb energy in the event of a crash, including automotive-sized front rails. Prepreg or fabric can easily be formed to tubular shapes and is the material of choice for the motorsport industry. Although no standard shape or dimension exists, either circular or square tubes have been traditionally employed; the latter having rounded corners [2]. The vast majority of the research conducted to determine the crush energy absorption of composite materials has focused on thin-wall tubular specimens [1-3]. Only a limited number of attempts have used test specimens of different geometries, and have included both self-supporting shapes, such as semicircular segments [4], channel stiffeners [5], corrugated webs [6], as well as flat plate specimens with dedicated anti-buckling fixtures [7]. The history behind the selection of tubular specimens can be attributed to several reasons: they are self-supporting, they do not require dedicated test fixtures, and they are ideally suited for both quasi-static and dynamic crushing.

On the other hand, the aerospace community has focused mostly on test specimens that resemble subfloor structures, such as floor beams, stanchions and stiffeners. These typically exhibit either a corrugated or channel shape, which are partially self-supporting, therefore do not require a dedicated test fixture, and are open sections, therefore they are more versatile from a manufacturing standpoint, and do not exhibit the hoop fiber constraint as tubular shapes. Bolukbasi and Laananen [5] conducted a systematic comparison of three structural configurations. Flat plates, angle sections, and C-channels were crushed under quasi-static conditions. Unidirectional tape was the material used, and two different lay-ups were considered. The NASA fixture described in [8,9] was used to provide anti-buckling support for the plate specimen. Although the number of specimens tested was limited, as was the selection of laminate lay-ups, it was found that the flat plates tested with the NASA fixture yielded higher SEA (Specific Energy Absorption) measurements than any of the self-supporting specimens, mostly attributable to the overly-constrained nature of the specimen. It was also shown that for both lay-ups tested, corner stiffeners yielded lower SEA than C-channel sections.

Numerical simulation has become a common tool in vehicle structural design, as well as in the certification stage. In particular, crashworthiness simulation plays a dominant role. A well-established simulation practice is needed to significantly reduce the amount of experimental testing required during product development and certification. Crash numerical codes are proven to properly simulate and predict the ductile deformation and progressive folding mechanism of sheet metal structures with minor occurrence of fracture [10]. Diversely, the behavior of composite materials under crash conditions poses particular challenges for engineering analysis since it requires modeling beyond the elastic region and into failure initiation and propagation. To date, the complexity associated with crush modeling of composite structures has been one of the most limiting factors in the widespread introduction of composites in the mainstream automotive industry [11]. With today's computational power it is not possible to capture each of the failure mechanisms that happen during a crash event [12].

Models based on lamina-level failure criteria have been used, although with well-accepted limitation [13] to predict the onset of damage within the laminate codes. Once failure initiates, the mechanisms of failure propagation require reducing the material properties using several degradation schemes [14]. To perform dynamic impact analysis, such as crash analysis, it is necessary to utilize an explicit finite element code, which solves the equations of motion numerically by direct integration using explicit rather than standard methods, for example using the central difference method [14]. Commercially available codes used for mainstream crash simulations include LS-DYNA, ABAQUS Explicit, RADIOSS and PAM-CRASH [15]. In general, these codes offer built-in material models for composites. Each material model utilizes a different modeling strategy, which includes failure criterion, degradation scheme, material properties, and usually a set of model specific input parameters that are typically needed for the

computation but do not have an immediate physical meaning. Composites are modeled as orthotropic linear elastic materials within the failure surface, whose shape depends on the failure criterion adopted in the model [14]. Beyond the failure surface, the appropriate elastic properties are degraded according to degradation laws. Depending upon the specific degradation law used, the constitutive models can be divided into either progressive failure models (PFM) or continuum damage mechanics models (CDM). Commercial software package LS-DYNA [16] offers a variety of material models for composite materials, which include both PFM (MAT22 and MAT54/55) and CDM (MAT58 and MAT162). The failure criteria for laminated composites in PFM are typically strength-based, and use a ply discount method to degrade material properties. At the failure surface, the values of the appropriate elastic properties of the ply in the material direction are degraded from the undamaged state, which is 1, to the fully damaged state, which is typically 0. The material model stress-strain curve does not require that a specific unloading/ softening curve be assigned, and after the strength of the ply is exceeded the properties are immediately dropped to zero. The so-called progressive failure is realized through ply-by-ply failure within the laminate, and once all plies have failed the element is deleted [16].

Currently, the large commercial transport aircraft industry utilizes a certification approach known as "certification by analysis supported by test evidence", or "allowables-based certification", to demonstrate compliance with regulatory Agency requirements, such as those of the Federal Aviation Administration (FAA). Margin of Safety calculations for static strength, durability and damage tolerance of composite materials are based on a complex mix of testing and analysis. This substantiation process is known as the Building Block Approach (BBA) [17-18]. It is recognized that analysis techniques alone are not sufficiently predictive for composites. However, by combining testing and analysis, analytical predictions are validated by test, test plans are guided by analysis, and the cost of the overall effort is reduced, while the degree of confidence and safety is increased.

In this paper, the merits and weaknesses of a progressive failure material model, MAT54, of a commercially available explicit finite element solver, LS-DYNA, are highlighted through single-element investigations. A comprehensive sensitivity study is performed on a single-element loaded in the principal direction: tension and compression, both in the fiber and matrix direction. By using LS-DYNA's MAT54, the quasi-static crushing of a composite specimen, consisting of a semi-circular sinusoid and manufactured with carbon/ epoxy unidirectional prepreg tape, is then modeled. The results are compared to the experimental evidence, whose details of the specimen design, manufacturing, and testing procedure have been previously published in [6]. In order to identify the effect of cross-section geometry on the overall crush behavior, both experimentally and numerically, five different specimen shapes are considered: a tube, a large and a small channel, and a large and a small corner. The goal is to isolate the SEA contribution of the corner detail from the total SEA of the section tested, both from an experimental and numerical standpoint. Finally, it is proposed in this paper to utilize the BBA, widely used in the aerospace community but often not utilized in the automotive industry, for the certification by analysis supported by test evidence by of an energy-absorbing structural concept for a high performance vehicle. Using this approach, it is shown that certification by analysis can be used successfully for simulating composite crushing and penetration.

Experimental Testing and Results

All carbon fiber specimens are manufactured by press-molding through a set of aluminum matching tools, and details are given in [6]. The material system is T700 carbon fiber/ 2510

epoxy prepreg, supplied by Toray Composites of America, comprising of a 270º F cure resin (132 ºC) designated for autoclave or oven-only cure. The first sinusoidal geometry specimen is considered using the unidirectional tape 12k tow material form. The lay-up is [0/90]$_{3s}$, yielding an average cured laminate thickness of 0.079 in. (2.0 mm). For the second sinusoidal specimen of the same geometry, but with different resulting thickness, and for the additional five shapes investigated, the material form is a flat woven 12k tow plain weave fabric. The lay-up considered is (0/90)$_{8s}$, yielding an average cured laminate thickness t 0.073 in (1.85 mm) for the sinusoidal specimen, and 0.065 in. (1.65 mm) for the additional five shapes. The T700 carbon fiber/ 2510 epoxy prepreg material is used extensively for General Aviation primary structures, and its properties are well documented as part of the FAA-sponsored AGATE Program (Advanced General Aviation Transport Experiment) [19, 20]. A summary of the material properties is provided for the unidirectional tape and the plain weave fabric, respectively, in Table I and II.

Table I. Material properties of T700/2510 Unidirectional tape as published in the CMH-17 [19, 20].

Property	Symbol	LS-DYNA Parameter	Experimental Value
Density	ρ	RO	0.055 lb/in^3 (1.52 g/cm^3)
Modulus in 1-direction	E_1	EA	18.4 Msi (127 GPa)
Modulus in 2-direction	E_2	EB	1.22 Msi (8.41 GPa)
Shear Modulus	G_{12}	GAB	0.61 Msi (4.21 GPa)
Major Poisson's ratio	v_{12}	-	0.309
Minor Poisson's ratio	v_{21}	PRBA	0.02049
Strength in 1-direction, tension	F_1^{tu}	XT	319 ksi (2.20 GPa)
Strength in 2-direction, tension	F_2^{tu}	YT	7.09 ksi (48. 9 MPa)
Strength in 1-direction, compression	F_1^{cu}	XC	213 ksi (1.47 GPa)
Strength in 2-direction, compression	F_2^{cu}	YC	28.8 ksi (199 MPa)
Shear Strength	F_{12}^{su}	SC	22.4 ksi (154 MPa)
Max strain for in tens. and comp. matrix	-	DFAILM	0.0240
Max shear strain	-	DFAILS	0.0300
Max strain for fiber tension	-	DFAILT	0.0174
Max strain for fiber compression	-	DFAILC	-0.0116

Table II. Material properties of T700/2510 Plain Weave Fabric as published in the CMH-17 [19, 20].

| Property	Symbol	LS-DYNA Parameter	Experimental Value
Density	ρ	RO	0.055 lb/in^3 (1.52 g/cm^3)
Modulus in 1-direction	E_1	EA	8.11 Msi (55.9 GPa)
Modulus in 2-direction	E_2	EB	7.89 Msi (54.4 GPa)
Shear Modulus	G_{12}	GAB	0.61 Msi (4.12 GPa)
Major Poisson's ratio	v_{12}	-	0.033
Minor Poisson's ratio	v_{21}	PRBA	0.043
Strength in 1-direction, tension	F_1^{tu}	XT	132 ksi (910 MPa)
Strength in 2-direction, tension	F_2^{tu}	YT	112 ksi (772 MPa)
Strength in 1-direction, compression	F_1^{cu}	XC	-103 ksi (-710 GPa)
Strength in 2-direction, compression	F_2^{cu}	YC	-102 ksi (-703 MPa)
Shear Strength	F_{12}^{su}	SC	19.0 ksi (131 MPa)
Max strain for in tens. and comp. matrix	-	DFAILM	0.01415
Max shear strain	-	DFAILS	0.0347
Max strain for fiber tension	-	DFAILT	0.01636
Max strain for fiber compression	-	DFAILC	-0.0129
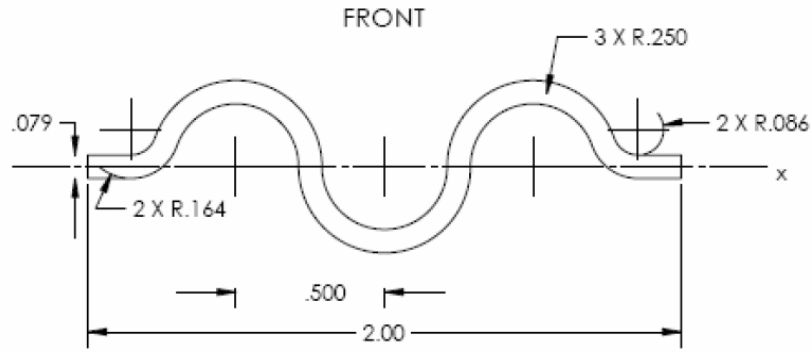
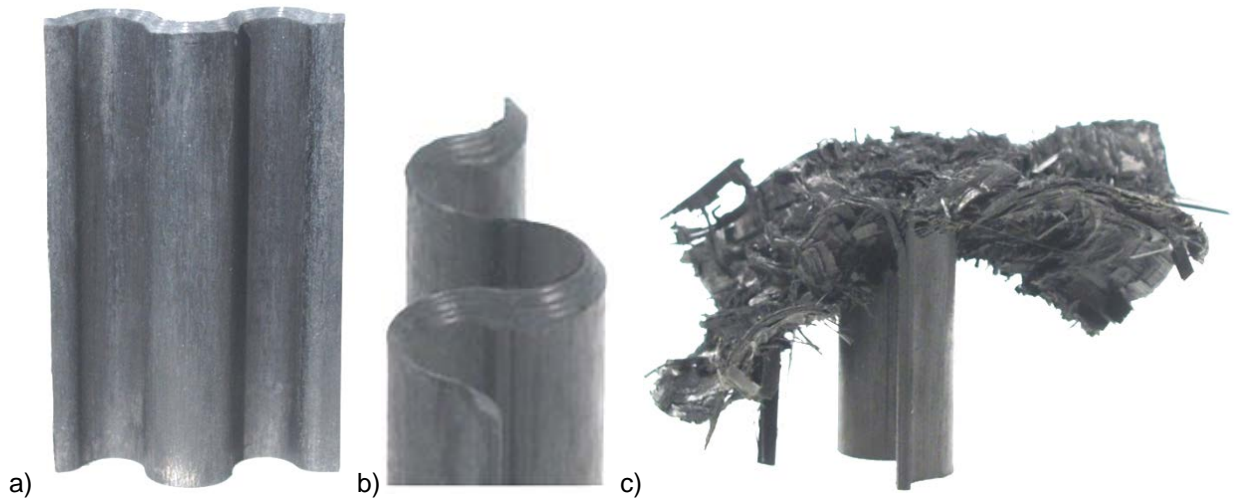*Figure 1: Cross section of corrugated coupon.*

Figure 2: a-c. Prepreg tape corrugated specimen (a), detail of the chamfered trigger (b), and typical morphology after crush testing (c).
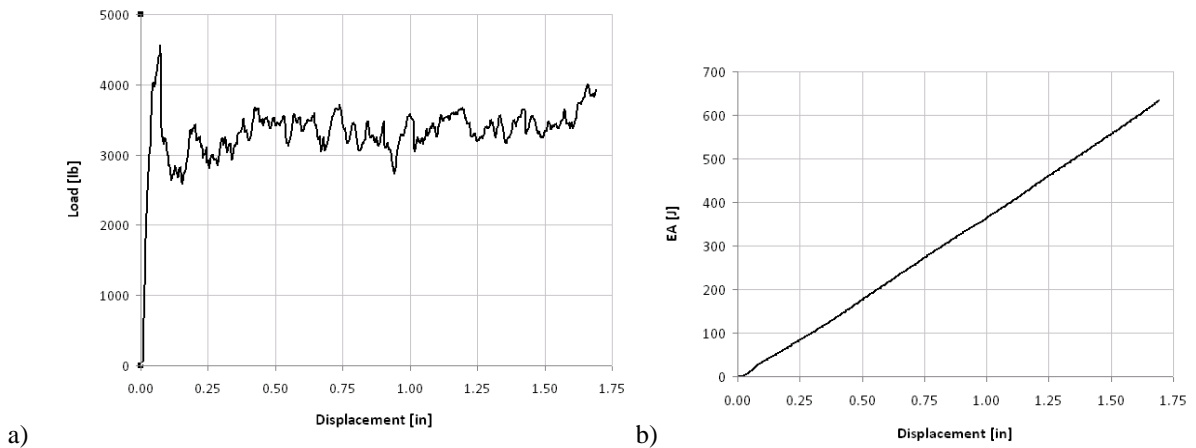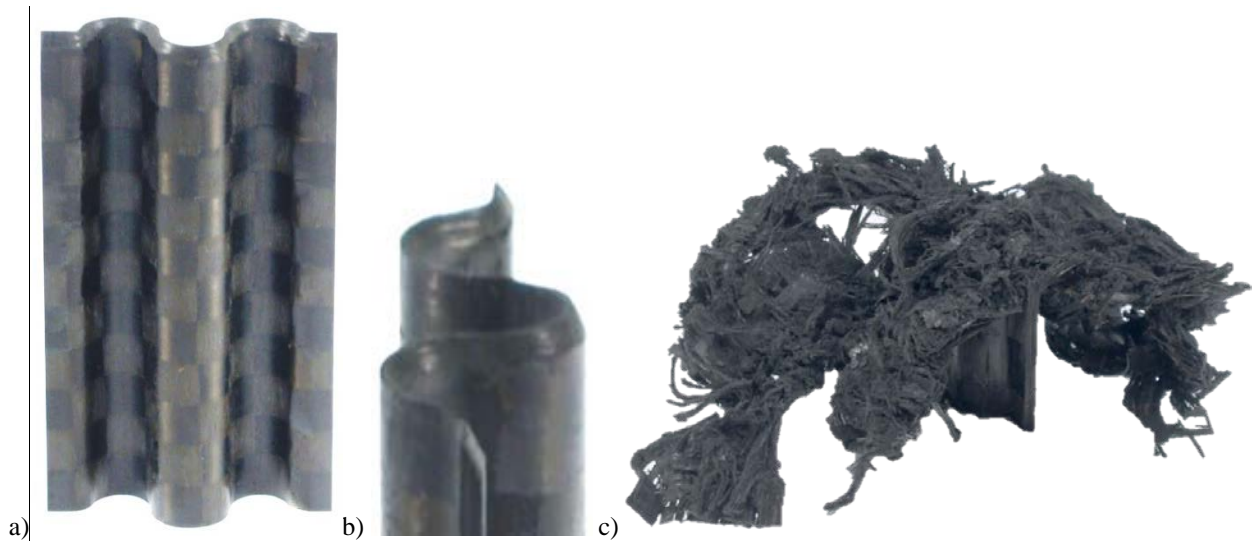

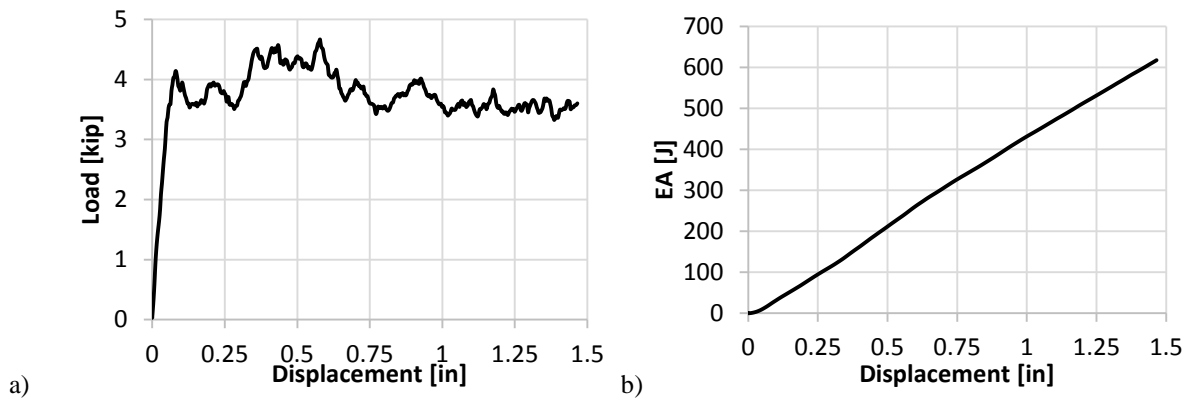*Figure 3 a-c. Experimental load-displacement curve (a), and total Energy Absorbed (b) as a function of displacement for the prepreg tape corrugated specimen.*

The upper end of the specimens are machined with a single-sided 45° chamfer to favor the initiation of stable crushing at the chosen end of the specimen, and to avoid undesired initial spikes in crush loads which may lead to specimen instability [7]. This chamfer is known as the

trigger, or crush-initiator. The specimens are tested in the vertical configuration, resting on a polished hardened steel surface, at a crosshead velocity of 1 in./ min (25.4 mm/ min.), which is noticeably below any dynamic effect reported for modern systems [1,6], approximately 40 in./sec (1.0 m/sec). Up to seven repetitions are used to obtain average data.

The sinusoidal specimen features a semicircular segment, of radius 6.4 mm (0.25 in.), repeated three times at alternating sides with respect to the mid-plane, Figure 1. The trigger is shown in Figure 2a-b and Figure 4a-b, respectively for the unidirectional tape and the plain weave fabric. Figures 3a-b and 4a-b show typical curves for a single test, in the order the load curve (a), and the total energy absorbed (b) as a function of displacement, respectively for the unidirectional tape and the plain weave fabric.

a)   b)   c)

Figure 4: a-c. Prepreg plain weave fabric corrugated specimen (a), detail of the chamfered trigger (b), and typical morphology after crush testing (c).

a)   b)

Figure 5 a-c. Experimental load-displacement curve (a), and total Energy Absorbed (b) as a function of displacement for the plain weave fabric corrugated specimen.

The measured SEA for the sinusoidal geometry for the unidirectional tape and plain weave fabric material forms is, respectively, 67.06 J/g and 88.98 J/g.

The entire load-displacement curves of Figure 2a and 5a (initial slope, peak load, and average crush load) and the average SEA value of Figure 2c and 5c are used as benchmarks

for comparing the success of the simulation results, respectively for the unidirectional tape and plain weave fabric material forms.
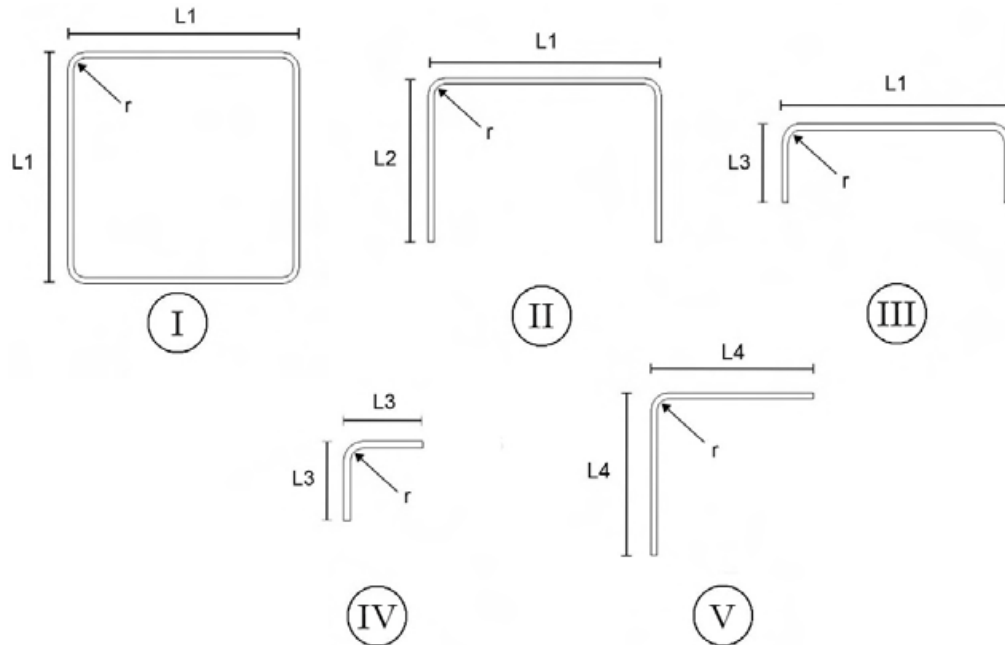

Figure 6. Sketch of cross-section shape and dimensions for all five geometries considered.

Table III. Summary of crush test results for all five specimen geometries.

Specimen No.	Shape	Peak Force (kN)	Average Crush Force (kN)	Crush Efficiency	Average SEA (J/g)	CoV (%)
I	Tube	39.9	23.8	1.68	36.9	10
II	Large Channel	21.6	13.0	1.66	36.8	9
III	Small Channel	17.1	10.7	1.60	42.7	3
IV	Small Corner	7.5	4.9	1.53	62.3	11
V	Large Corner	15.3	9.4	1.63	31.6	8

Table IV. Summary of the five specimens considered and associated key geometry.

Specimen No.	Shape	Outer Dimensions	Section Length	Portion of cross section affected by one corner, S_i	Remaining portion of the cross-section, ΔS
I	Tube	L1xL1	S_I	¼ S_I	$2\Delta S'$
II	Large Channel	L1xL2	S_{II}	½ S_{II}	$\Delta S' + \Delta S''$
III	Small Channel	L1xL3	S_{III}	½ S_{III}	$\Delta S'$
IV	Small Corner	L3xL3	S_{VI}	S_{VI}	0
V	Large Corner	L4xL4	S_V	S_V	$2\Delta S'''$

Using an aluminum square tubular mandrel, the square tube is extracted from the mold. After trimming, the length of the specimen is 3.5 in. (88.9 mm). The radius of the mandrel, and hence the inner radius r of the tube, is 0.175 in. (4.45 mm). The cross section of the tube has outer dimensions L1 x L1 (Figure 6, I) and a total perimeter of S_I. In order to obtain the other

four shapes considered in this study, a portion of the square tube specimens are cut with a diamond-coated disk saw. With a single cut performed off-axis on the square cross-section the large and the small C-channel sections are obtained. The large C-section has dimensions L1 x L2, while the small C-channel has outer dimensions L1 x L3, where L3 is the given by L1-L2 (Figure 6, II and III). The total perimeters for the large and small C-channels are indicated as S_{II} and S_{III} respectively. In order to obtain the fourth specimen, a second cut is performed on a portion of the small C-channels previously obtained. The cut is performed off-axis, and it enables for isolating a single corner element. The small corner element has outer dimensions L3 x L3 (Figure 6, IV), and a perimeter indicated by S_{IV}. The fifth and last specimen, the large corner element, is obtained by performing two cuts on the original square section I, in the proximity of two opposing corners. The specimen has outer dimension L4 x L4 (Figure 6, V), and section length S_V. Tables III and IV shows in detail the list of parameters introduced and the associated numerical values. All section specimens except of the tube and the sinusoidal shape are potted into an epoxy resin base in order to provide stability during crashing; hence their effective length is reduced by at 0.5 in (12.5 mm). Tables VI and V show in detail the list of parameters introduced and the associated numerical values.

Table V. Summary of parameters and associated numerical values used in this study.

Parameter	Value
L1	2.50 in. (63.5 mm)
L2	1.75 in. (44.5 mm)
L3	0.75 in. (19.0 mm)
L4	2.00 in. (50.8 mm)
r	0.175 in. (4.45 mm)
t	0.065 in. (1.65 mm)
S_I	10.50 in. (266.7 mm)
S_{II}	5.75 in. (146.0 mm)
S_{III}	3.75 in. (95.3 mm)
S_{VI}	1.25 in. (31.75 mm)
S_V	4.50 in. (114.3 mm)
$\Delta s'$	0.75 in. (19.0 mm)
$\Delta s''$	1.00 in. (25.4 mm)
$\Delta s'''$	1.60 in. (40.6 mm)
ρ	1.52 g/ cm^3

All of the five additional shapes tested in this study crush in a stable manner, Figures 7-11, exhibiting frond formation and bending, particularly specimens II-V. The square tube, specimen I, exhibits an accordion-type of crushing, comprised of a succession of local segments folding on each other. It should be observed that the predominant failure mode at the corner is tearing fracture of the woven fiber tows, while in the flat segments it is lamina bending of the fronds. The SEA values for each additional shape are summarized in Figure 12, while the summary of the test results are reported in Table III. For each of the specimen geometries listed, six repetitions are performed, and the variation among these repetition is capture via the Coefficient of Variation (CoV).
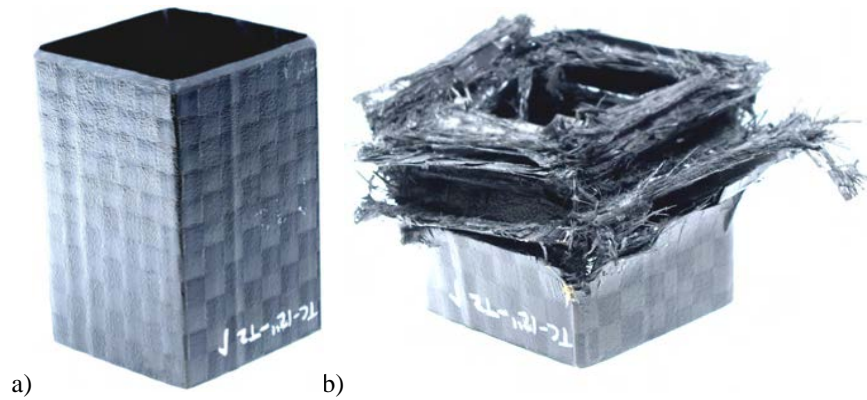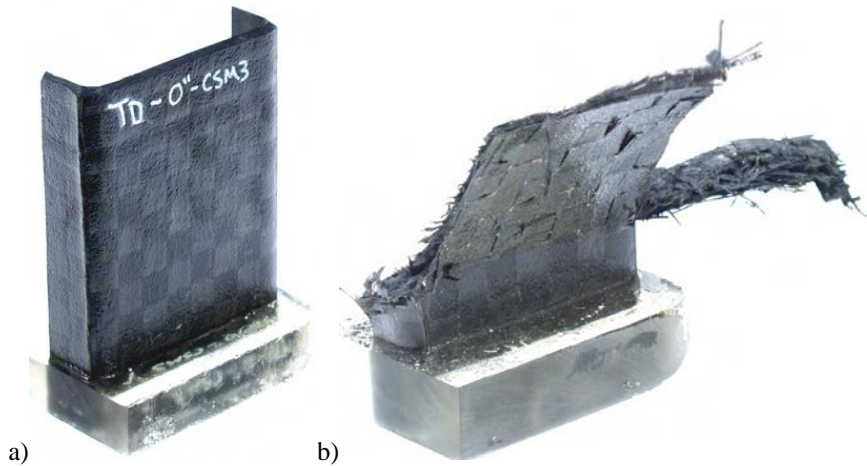
a)   b)

Figure 7. Square tube, specimen I, before and after crush testing.
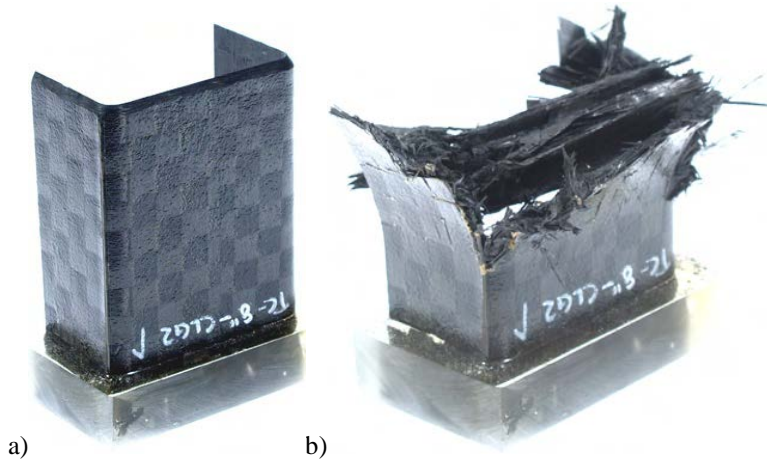
a)   b)

Figure 8. Large C-Channel, specimen II, before and after crush testing.

a)   b)

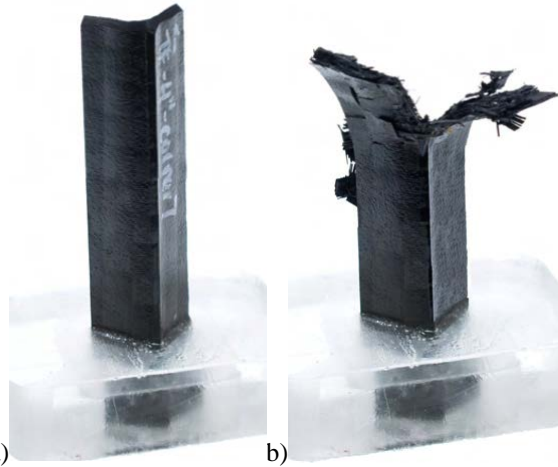*Figure 9. Small C-Channel, specimen III, before and after crush testing.*

a)   b)

Figure 10. Small corner element, specimen IV, before and after crush testing.
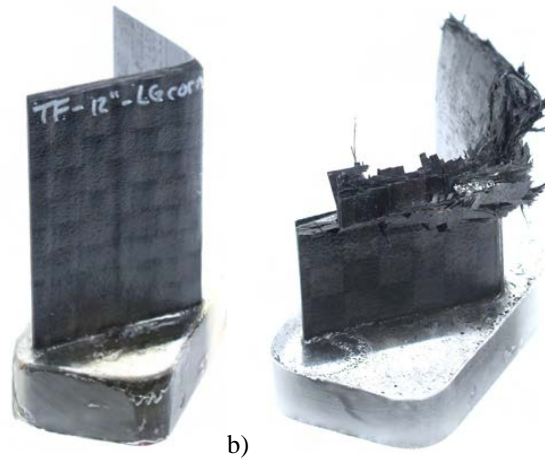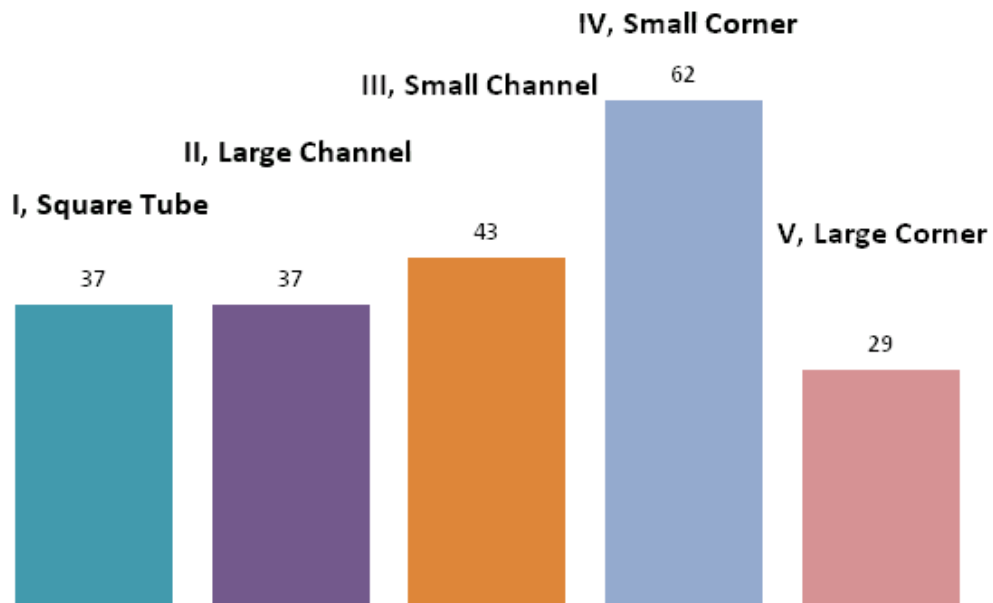

a)   b)

Figure 11. Large corner element, specimen IV, before and after crush testing.

Figure 12. Summary of average SEA results in J/g for all five additional shapes tested.

Interpretation of the Experimental Results

When analyzing the energy absorption behavior of a structure, a few key definitions are required:

- Peak Force - the maximum point on the Force-Stroke diagram.

- Average Crush Force - the displacement-average value of the force history.

- Crush Efficiency - the ratio of peak force to average crush force.

- Stroke (δ)- the length of structure/material being sacrificed during crushing.

- Energy Absorbed (EA) - The total area under the Force-Stroke diagram.

- Specific Energy Absorption (SEA) - The energy absorbed per unit mass of crushed structure.

The ability of a material to dissipate energy can then be expressed in terms of SEA, which has units of J/g, and indicates a number, which for composites is usually comprised between 15 and 100 J/ g. Setting the mass of structure that undergoes crushing as the product of stroke δ, cross-sectional area A, given by the product of thickness t and section length S, and density ρ:

$$\text{SEA} = \frac{\text{W}}{\rho \cdot \text{A} \cdot \partial} = \frac{\int_0^{\partial} \text{F} \cdot \text{d} \partial}{\rho \cdot \text{t} \cdot \text{S} \cdot \partial} \tag{1}$$

The sinusoidal specimen measured a higher SEA with the plain weave fabric material form: 88.98 J/g versus 67.06 J/g of the unidirectional tape. The progressive crushing behavior can be sub-categorized as a combination of the splaying and fragmentation failure modes [1, 22]. Splaying is characterized by very long interlaminar, intralaminar, and parallel-to-fiber cracks with little or no fracture of axial bundles, while fragmentation is characterized by a wedge-shaped laminate cross-section, with one or more short interlaminar and longitudinal cracks forming partial lamina bundles. The wedge-shaped section is created by the growth of the interlaminar cracks which eventually cause the edges to fracture. The primary energy absorption mechanism of splaying is crack growth, while of fragmentation is fracture of the lamina bundles. Fragmentation is the failure mode which is responsible for the majority of the energy absorption that occurs during progressive crushing. It is believed by the authors that more fragmentation and less splaying occur with a plain weave fabric, when compared to a unidirectional tape material form.

Each of the additional five sections considered in this study is comprised of one or more corner details, and additional segments of flat material. If the small corner detail, specimen IV, is used as the repetitive unit, each cross-section can be subdivided into half- or quarter- sections that are influenced by a single corner detail, as tabulated in the right hand column on Table III. It becomes therefore possible to measure the SEA and crush behavior of a stand-alone corner element, and then extrapolate the actual in-situ SEA and crush behavior of the flat sections, which is otherwise difficult to assess experimentally [7-21].

To that extent, the square tube cross-section can be subdivided in a quarter-section, comprised of the corner detail of perimeter S_{IV}, and two additional flat segments on both sides of the corner, each of length ΔS' (Figure 13, I). This quarter section represents the portion of the square cross-section that is influenced by a single corner detail, since the double symmetry accounts for the other three corner elements. For the large C-channel, the half-section comprises the corner detail of perimeter S_{IV}, same as the corner element specimen, and two additional flat segment of total length ΔS' and ΔS'' (Figure 13, II). This half section represents

the portion of the large C-channel cross-section that is influenced by a single corner detail, since symmetry accounts for the other corner element. Similarly, the small C-channel can be subdivided into a half-section, comprised of the corner detail of perimeter S_{IV}, same as the corner element specimen, and one additional flat segment of length $\Delta S'$ (Figure 13, III). Lastly, the large corner element can be also subdivided into a small corner element of perimeter S_{IV}, and two additional flat segments, each of length $\Delta S'''$ (Figure 13, V).
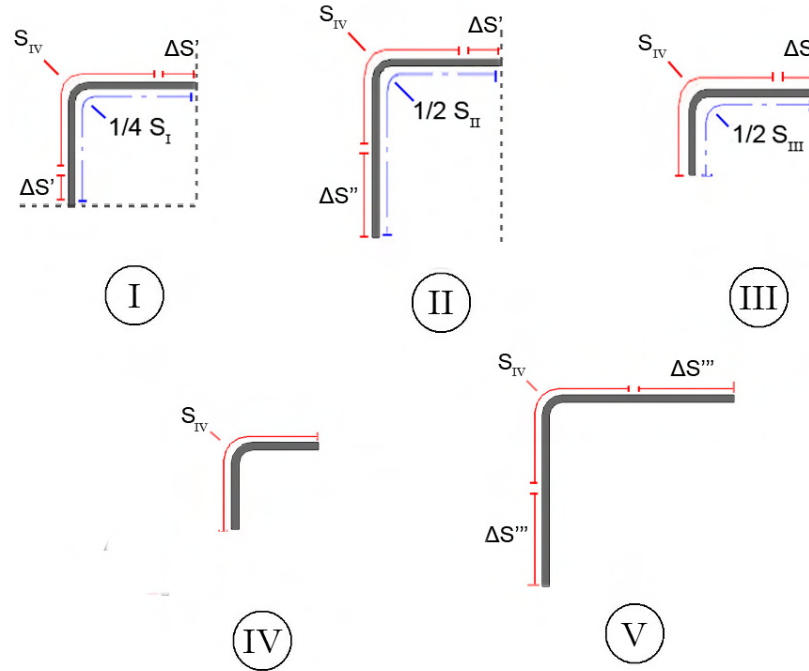
Figure 13. Subdivision of section length into a corner detail and portion of flat segment, for each of the five specimen cross-section geometries considered.

The remaining portion of the cross-section is comprised of flat segment after subtracting the small corner, ΔS, is then defined by the following equation:

$$\Delta S = S_i - S_{IV} \qquad (2)$$

The values of Si and ΔS for each of the five shapes as a function of S_I, S_{II}, S_{III}, $\Delta S'$, $\Delta S''$ and $\Delta S'''$ are tabulated in Table III, respectively in column 3 and 4. The numerical values for S_I, S_{II}, S_{III}, $\Delta S'$, $\Delta S''$ and $\Delta S'''$ are listed in Table IV.

In general, it can be seen from Figure 12 that the small corner element exhibits a much higher SEA than the other specimens, followed by the small and large C-channels, the square tube and, lastly, the large corner element. The small corner, exhibiting the least amount of flat segments in its cross section, is therefore the most efficient in dissipating energy per unit mass of material crushed, and this can be attributed to the tearing failure mechanism observed. On the other hand, the large corner is the least efficient, exhibiting the most amount of flat segments in its cross section, and this can be attributed to the frond bending failure mechanism observed. The SEA_i for each shape can be subdivided into two components, one associated with the corner detail, obtained from testing a corner element and denoted SEA_{IV}, and one associated to the remaining flat segments, and denoted SEA_f. These SEA contributions are weighed based on the ratio of the lengths of corner detail (S_{IV}) with respect to the total length of the section (S_i), and of the remaining flat segments (ΔS) with respect to the total length of the section (S_i):

$$SEA_i = \left(\frac{S_{IV}}{S_i}\right) SEA_{IV} + \left(\frac{\Delta S}{S_i}\right) SEA_f \tag{3}$$

If Eq. 3 is solved for the unknown value of SEAf since all other quantities are either known or can be measured experimentally, it is possible to extrapolate the in-situ value of the SEA associated with flat sections, like the ones that form the fronds observed in splaying failure. The average value obtained this calculation is SEAf = 16.3 J/g, which is much lower than the average SEAIV = 62 J/g recorded during the crushing of the corner elements. Although there is evident variation in the results, it is consistent with the CoV measured between repetitions. In conclusion, although the corner element exhibits a higher measured SEA than any of the other shapes tested, the contribution of the flat sections cannot be neglected.

From the study it is possible to note that the degree of curvature greatly influences the energy absorption behavior: the more contoured the specimen cross-section, the higher the energy dissipated per unit mass of material. This observation becomes evident in Figure 20, which plots the variation of SEA with respect to the dimensionless index φ, which is an indicator of the degree of curvature of the cross-section, and is given by:

$$\emptyset = \frac{l}{S_i} = \frac{\pi \cdot r}{2 \cdot S_i} \tag{4}$$

where l is the arc length, given by the product of the radius r and the angle π/2, and S_i is length of the cross section influenced by the corner, as defined in Table IV.

Segments of cross-section characterized by changes in curvature, such as corners, are much more efficient in absorbing energy than sections with long flat segments, as shown in Figure 14, where there appears to be a linear trend between SEA and the dimensionless parameter φ.
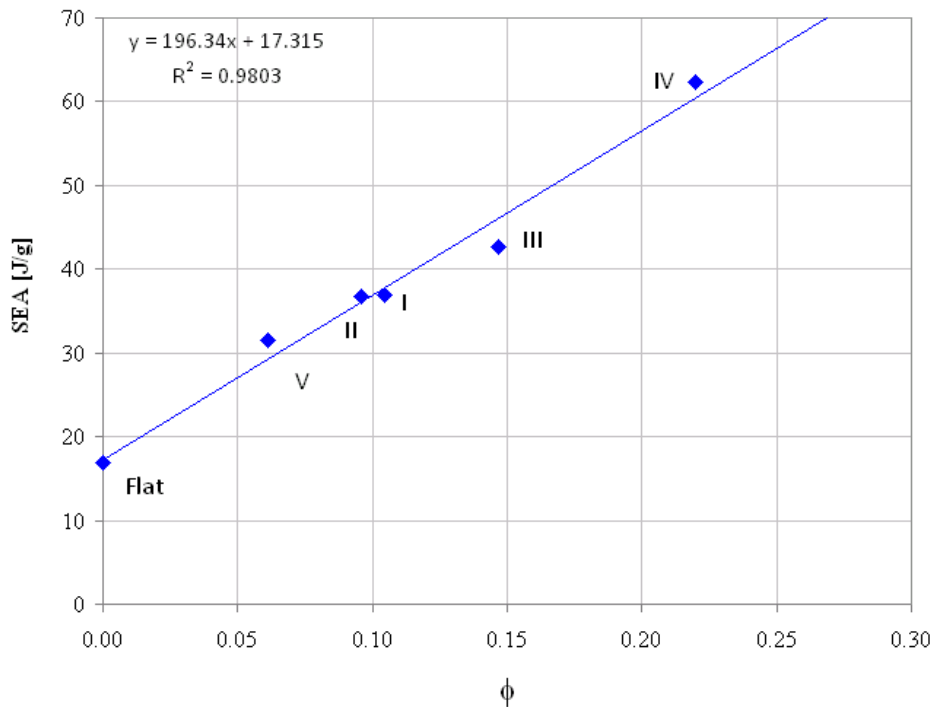

Figure 14. SEA variation with φ, which is an indicator of curvature per unit length of cross-section for all specimens tested.

Analytical Results

MAT54 material model is a progressive failure model within the commercial software LS-DYNA, which uses the Chang-Chang failure criteria to determine individual ply failure. Failure can occur when one of the following strength criteria is exceeded [16,23-24]:

$$e_f^2 = \left(\frac{\sigma_{11}}{F_1^{tu}}\right)^2 + \beta\left(\frac{\sigma_{12}}{F_{12}^{tu}}\right)^2 \begin{cases} \geq 1 \; failed \\ < 1 \; elastic \end{cases} \tag{5}$$

Upon failure: $E_1 = E_2 = G_{12} = v_{12} = v_{21} = 0$

$$e_c^2 = \left(\frac{\sigma_{11}}{F_1^{cu}}\right)^2 \begin{cases} \geq 1 \; failed \\ < 1 \; elastic \end{cases} \tag{6}$$

Upon failure: $E_1 = v_{12} = v_{21} = 0$

$$e_m^2 = \left(\frac{\sigma_{22}}{F_2^{tu}}\right)^2 + \left(\frac{\sigma_{12}}{F_{12}^{tu}}\right)^2 \begin{cases} \geq 1 \; failed \\ < 1 \; elastic \end{cases} \tag{7}$$

Upon failure: $E_2 = v_{12} = G_{12} = 0$

$$e_d^2 = \left(\frac{\sigma_{22}}{2F_{12}^{su}}\right)^2 + \left[\left(\frac{F_2^{cu}}{2F_{12}^{su}}\right)^2 - 1\right]\frac{\sigma_{22}}{F_2^{cu}} + \left(\frac{\sigma_{12}}{F_{12}^{su}}\right)^2 \begin{cases} \geq 1 \; failed \\ < 1 \; elastic \end{cases} \tag{8}$$

Upon failure: $E_2 = v_{12} = v_{12} = G_{12} = 0$
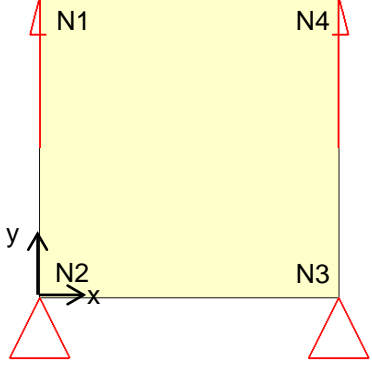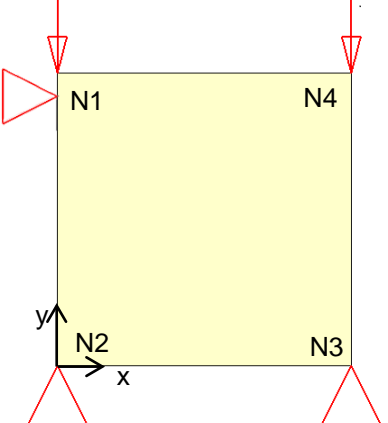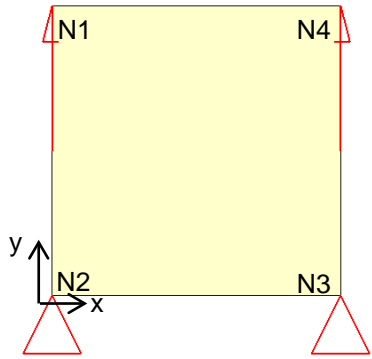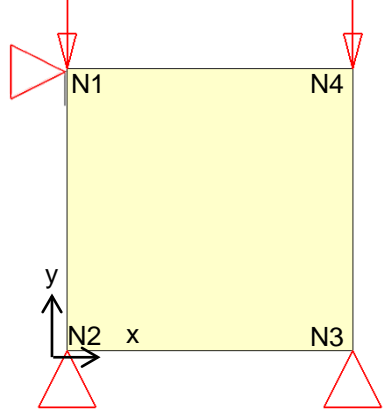
Table VI. Additional MAT54 input parameters for both material forms.

Symbol	Title	Value
SOFT	Crash front parameter	…
Alpha	Shear stress parameter for nonlinear terms	0.3
Beta	Weighting factor for shear term in tensile fiber mode	0.5
TFAIL	Time step size criteria for element deletion	1.153E-9
Shell Element size	In.	0.1

The LS-DYNA parameters, and the material properties they represent, are listed in Tables I and II, respectively for the unidirectional tape and plain weave fabric material forms. When one of the above conditions is exceeded in a ply within the element, all specified elastic properties of that ply are set to zero. The input parameters in the material model that are not material properties are listed in Table VI for both material forms. All parameters are kept constant between the models of the various geometries, except for the SOFT parameter, as described subsequently. Beside the Chang-Chang strength criterion, a ply can be removed when the strain exceeds one of the ultimate strains. A ply can also be removed if failure does not occur by any of the above reasons within a cycle time smaller than TFAIL, and the element is eliminated by time out. The other parameters described in Table VI are:

- SOFT is the crash front parameter. It is a softening reduction factor for material strength in the row of elements immediately following that currently undergoing crushing. The default value is 1, which means that the elements are pristine, or retain 100% of their strength. A SOFT value of 0.6 indicates that the row of elements following the crashfront is set to retain only 60% of the pristine strength. It acts as a damage zone by assuming that the row of elements right after to the crashfront undergoes a partial state of damage even before it becomes the crashfront.

Table VII. Summary of single-element models

Model	Load Case	Lay-up	B. C's	Load. Condition
	Fiber tension	$[0]_{12}$	Fixed displacements: N2: Y, Z, X N3: Y, Z	N1 & N4: Applied 2 [in/s] linear motion in positive y-direction
	Fiber compression	$[0]_{12}$	Fixed displacements: N1: X, Z N2: X,Y,Z N3: Y, Z N4: Z	N1 & N4: Applied 2 [in/s] linear motion in negative y-direction
	Matrix tension	$[90]_{12}$	Fixed displacements: N2: Y, Z, X N3: Y, Z	N1 & N4: Applied 2 [in/s] linear motion in positive y-direction
	Matrix compression	$[90]_{12}$	Fixed displacements: N1: X, Z N2: X,Y,Z N3: Y, Z N4: Z	N1 & N4: Applied 2 [in/s] linear motion in negative y-direction

- Alpha is the shear stress parameter for the nonlinear term.

- Beta is the weighting factor for shear term in tensile fiber mode. It ranges from 0 to 1. For β = 1, the failure criteria of Hashin [24] is applied in the fiber tensile mode. When β = 0, Equation 5 reduces to the maximum stress criterion.

MAT54 is designed specifically to handle orthotropic materials such as unidirectional tape composite laminates, but not fabrics. However, MAT54 is often utilized to model a fabric or non-unidirectional tape material form [25-26].
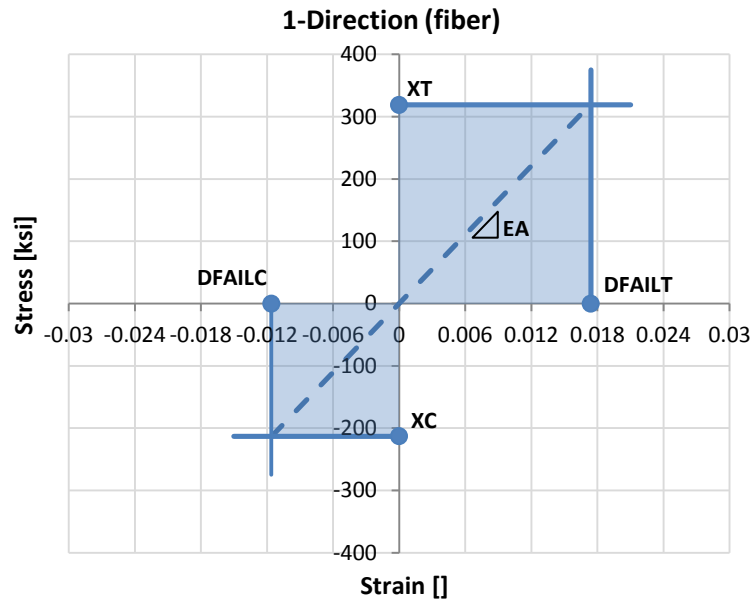
a)
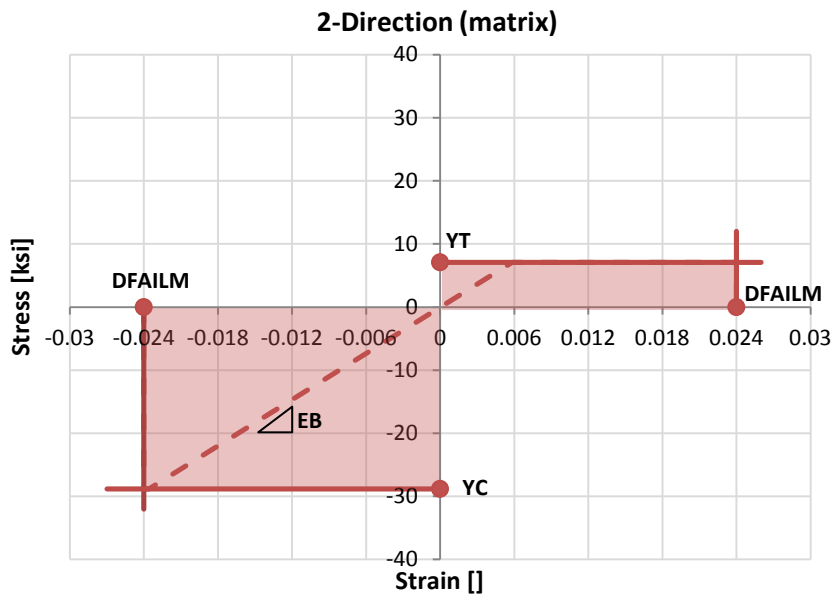
b)

Figure 15 a-b. Material stress-strain envelopes in the 1- (a) and 2- (b) directions as interpreted by the MAT54 input parameters for the unidirectional tape material form.
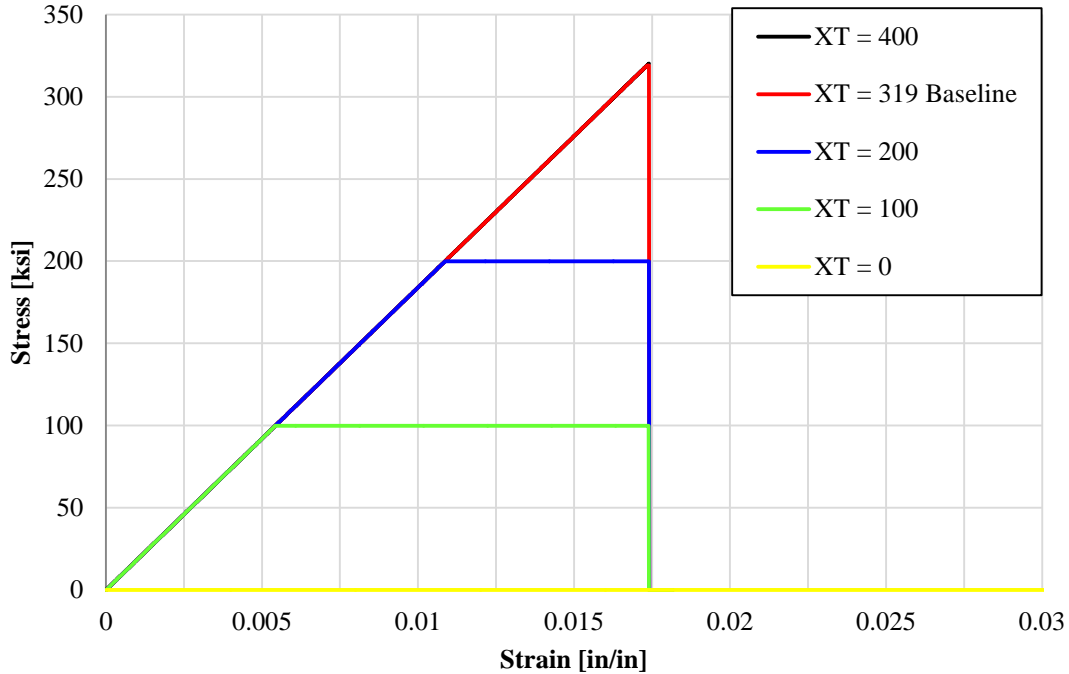
Figure 16. Effect of changing the tensile strength, XT, on the baseline simulation.

A 0.1 in. x 0.1 in. single-element model is developed to investigate the failure behavior of MAT54 by using four different boundary and loading conditions which are designed to isolate the failure modes, Table VII. At a single-element level, a comprehensive investigation is performed on the capability of MAT54. While the MAT54 material cards has separate parameters for the tensile and compressive strain to failure in the fiber direction, respectively called DFAILT and DFAILC, a single material card parameter is offered for both the tensile and compressive matrix strain to failure. For a unidirectional tape, these values are significantly different and the user is obligated to use the higher one of the two to define the DFAILM parameter in order to avoid premature and erroneous element deletion in the matrix compression loading direction. This however results in the modeling of a large perfectly plastic segment in the stress-strain envelope in the material 2-direction, as shown in Figure 15b. Ply failure only occurs by one of the stress criteria, while element deletion is only obtained by one of the strain criteria, Figure 16 and 17. In the LS-DYNA user manual it is not clearly explained that when failure occurs in a ply, the stress-strain behavior becomes perfectly plastic until deletion occur, Figure 17. This phenomenon becomes particularly evident when modeling a [0/90]$_{ns}$ tape lay-up, as shown in Figure 18. After failure, the element deletion occurs much later, only when the 90° plies reach the matrix strain to failure. In this case, failure occurs at 0.0174 strain, while the element is deleted at 0.024 strain, Figure 19. This is in contract with the physical behavior where, when the 0° plies fail, a composite specimen fractures.

Among others the parameters investigated are mesh size, loading speed and time step size. An interesting and preliminary result is that the optimal mesh size for MAT54 is discovered to be around 0.1 in. Mesh size values significantly lower or higher result in erroneous results.
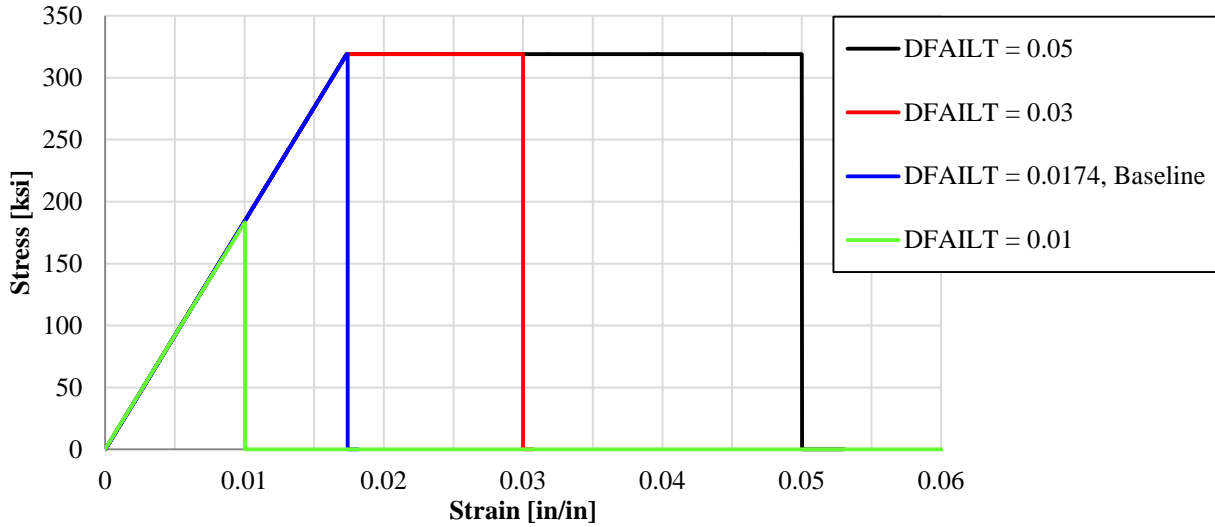
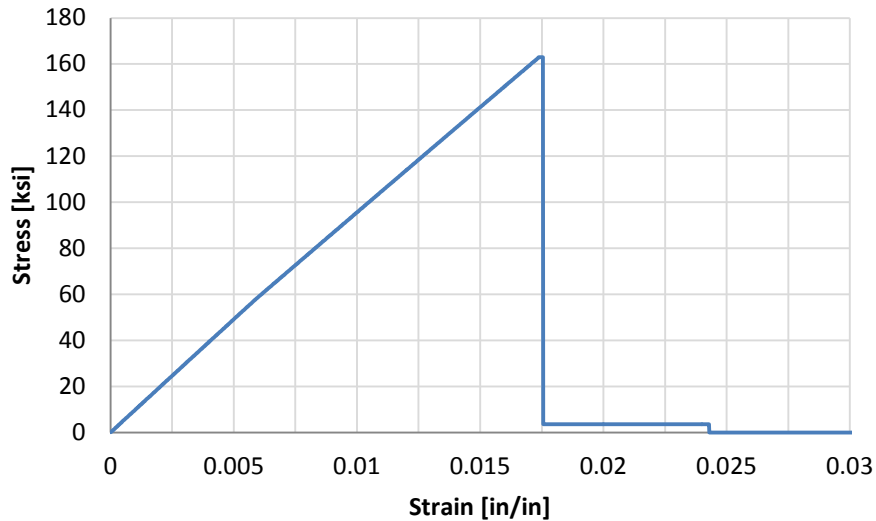Figure 17. Effect of changing the tensile strain to failure,DFAILT, on the baseline simulation.

Figure 18. Tensile baseline simulation for a [0/90]$_{3s}$ single-element model

After having identified the limits and merits of the MAT54 material model, a model is built to simulate the crush behavior of the half-circular sinusoidal specimen. The LS-DYNA model is represented in Figure 20 and shows the loading plate, the composite specimen and the trigger row. The geometry is imported into LS-DYNA and meshed using a fully integrated linear shell element (formulation 16) of 0.1 in x 0.1 in. (2.54 mm x 2.54 mm) square element size. The trigger is modeled as a single row of reduced thickness (0.01 in or 0.25 mm) elements at the crush front of the specimen. The specimen is kept at rest by constraining all degrees of freedom using a nodal single point constraint (SPC) boundary condition on the bottom row on nodes opposite the crush trigger. A large single shell element perpendicular to the specimen crush front is used to model the loading plate. The loading plate is modeled as a rigid part (undeformable) with properties of a steel using MAT20. The ENTITY and RIGID_NODES_TO_RIGID_BODY contact algorithms are utilized to define the contact interaction respectively when using the unidirectional tape and plain weave fabric material forms.
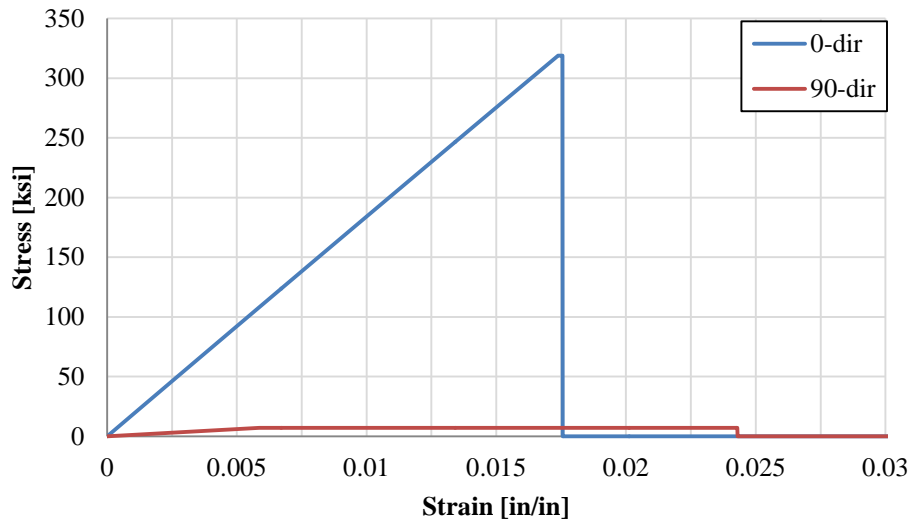
Figure 19. Stress is the loading direction in the 0° and 90° direction plies of a [0/90]₃ₛ single-element model.

The ENTITY contact algorithm better represents the initial slope of the numerical load-displacement curve, however when utilizing a plain weave fabric material system, instabilities are encountered while performing a parametric sensitivity investigation. The RIGID_NODES_TO_RIGID_BODY contact algorithm results in a slower initial response of the numerical simulation, but guarantees stability in all cases. In both cases, a piecewise linear (PCWL) load penetration (LP) curve is utilized to define the reaction normal force applied to each node as function of the distance the node has penetrated through the surface that is contacting.
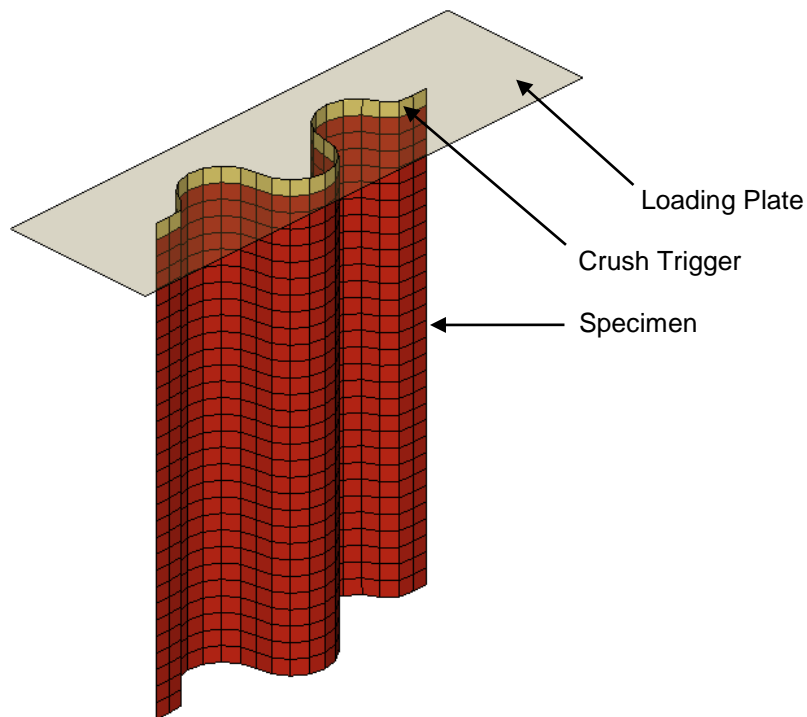
Figure 20. LS-DYNA model of the corrugated composite specimen, crush trigger, and loading plate.

Although the true experimental crush loading rate is 1.0 in./ min. (25.4 mm/min), simulations are performed using a crush velocity of 150 in./sec (3,810 mm/sec) because of computational runtime limitations. Since all material properties were measured with quasi-static tests, no strain-rate dependent material properties were defined in the input deck (material card); hence the model cannot assume strain-rate behavior. It is verified that inertial effects do not arise by carrying out simulations at lower speed and noticing no difference in results.

| t = 0.00 [s] | t = 0.002213 [s] | t = 0.004543 [s] |
| t = 0.006873 [s] | t = 0.009203 [s] | t = 0.01153 [s] |
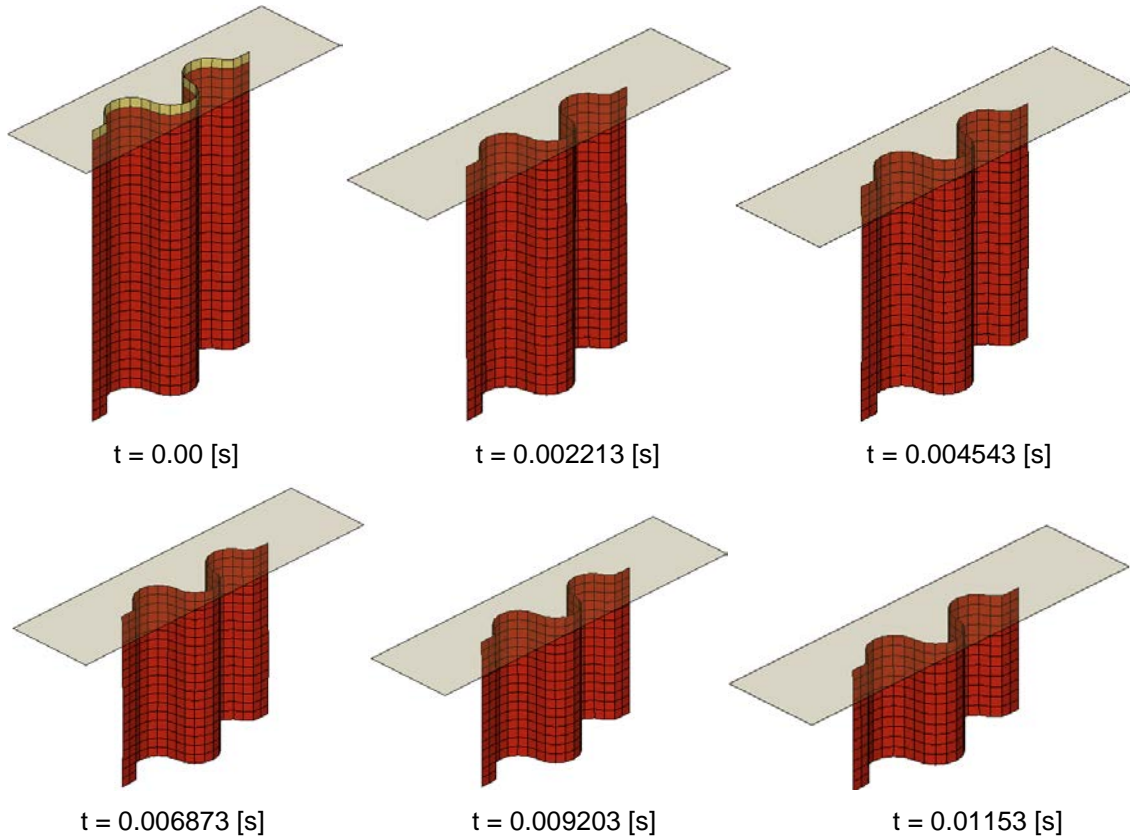
Figure 21. Time progression of the baseline simulation showing stable element row deletion.

The time progression of the baseline simulation, Figure 21, reveals that failure advances in an even and stable fashion, through the element deletion at the crush front. When the first ply in an element fails, the element remains in the straight position and does not exhibit a different morphology. Once all plies have failed, the element is immediately deleted. Once an element is deleted, the entire row of elements is also deleted. Therefore crush progresses with a progressive deletion of the crush front row of elements without any other graphic indication. It is an unfortunate characteristic of MAT54 to not allow for elements to bend forming fronds, regardless of what actually happens in the physical world, Figures 2c and 4c.

The load-displacement curve obtained from the model is shown in Figure 22 in its raw and filtered state. The raw curve is characterized by an alternating series of sharp peaks and valleys, giving it a saw tooth look. This feature is a typical result of the mathematical model, which is linear up to failure at the peak, then drops to zero upon deletion of the current row of elements, until the next row of elements picks up the load again. It is common practice to filter the numerical results using a low-pass digital filter (SAE 600 Hz) during post-processing [14-15, 27]. Through filtering, the average crush load remains unchanged, but the peaks and valleys are smoothed. The curve oscillates about the average crush load without large variations in local peak values, indicating that the simulation is stable.
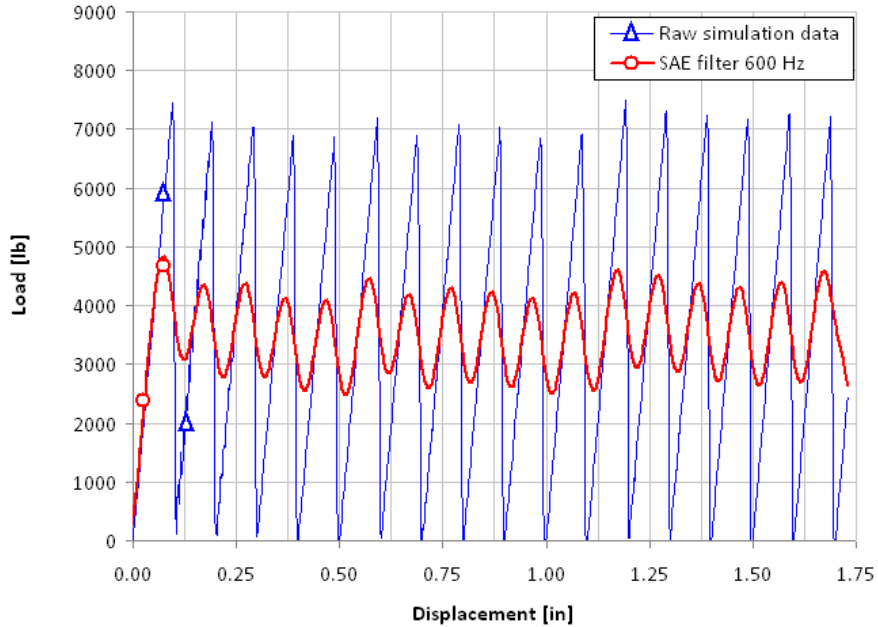
Figure 22. Filtered versus raw numeric crush data from the baseline simulation.

The simulation captures all key characteristics of the experimental curve: initial slope, peak load, and average crush load, which in turn is used to compare the SEA value of the simulation to the experimental measure SEA value. The comparisons between the experimental and numerical load-displacement curves are shown in Figure 23 and 24, respectively for the unidirectional tape and plain weave material forms. The differences between the two models are the material properties, the element lay-up (the plain weave fabric plies are all oriented in the 0° direction), the contact definition and the SOFT parameter. The SOFT parameter is set to 0.57 and 0.6, respectively for the unidirectional tape and plain weave material forms. The value of the SOFT is obtained by trial-and-error.
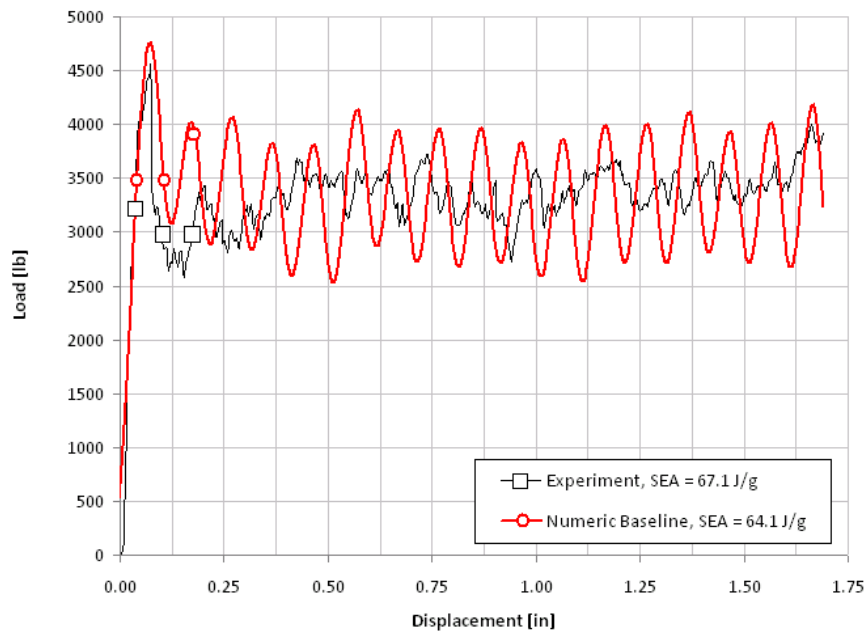

Figure 23. Experimental and model baseline load-displacement curves for the unidirectional tape material form.
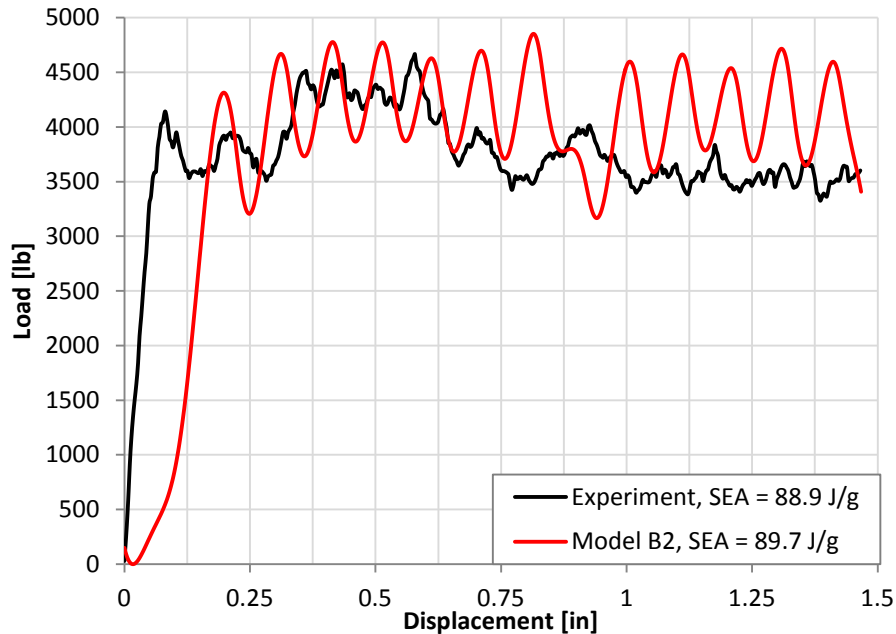
*Figure 24. Experimental and model baseline load-displacement curves for the plain weave fabric material form.*

Once it is demonstrated that MAT54 can be used to simulate the behavior of the sinusoidal specimen with both material forms, the numerical investigation is expanded to the five additional shapes. When the same material card of the plain weave fabric sinusoidal model is utilized for each of the five additional shapes, the results are not found to be stable and Euler buckling is the dominant failure mechanisms. It is found that the value assigned to the SOFT parameter has the most dramatic influence on the overall simulated crush response. For SOFT values that are too high, which means that the strength of the element row following the crush front is not reduced enough, crushing is not stable. Upon loading, stress builds up and eventually leads to failure at a point away from the crush front. For SOFT values that are too low, the elements are deleted prematurely and the resulting sustained crush load is lower than the experimental. By performing a trial-and-error procedure on each geometrical shape, a suitable SOFT parameter value to match the experimental curves for all five shapes is found. It is seen that although the material for these shapes is the same, the value of the SOFT parameter has to be varied for each shape in order to capture the experimental data. This bears the dual implication that the SOFT parameter is not a constant of the material, and that it cannot be predicted a priori. This in turn also means that LS-DYNA MAT54, although can be used successfully to reproduce the experimental results, it does not allow for a true predictive capability.

Summarized in Table VIII are the values of SEA measured and simulated for each geometry, as well as a summary value of the optimal SOFT value as determined by trial-and-error. Figure 25 show the detailed geometry as well as the experimental and simulated L-D curves for all specimens considered.

Rearranging the values in Table VIII it is possible to plot the experimental, and numerical, values of the SEA for each of the five geometries considered against the respective values of the SOFT parameter, Figure 26. It is very interesting to observe that there is a striking relationship between the SEA and this parameter, generally thought of as a numerical "tweaking" parameter. The relationship appears to be linear, and bears a strong connection to the plot of Figure 10, which shows SEA against degree of curvature.
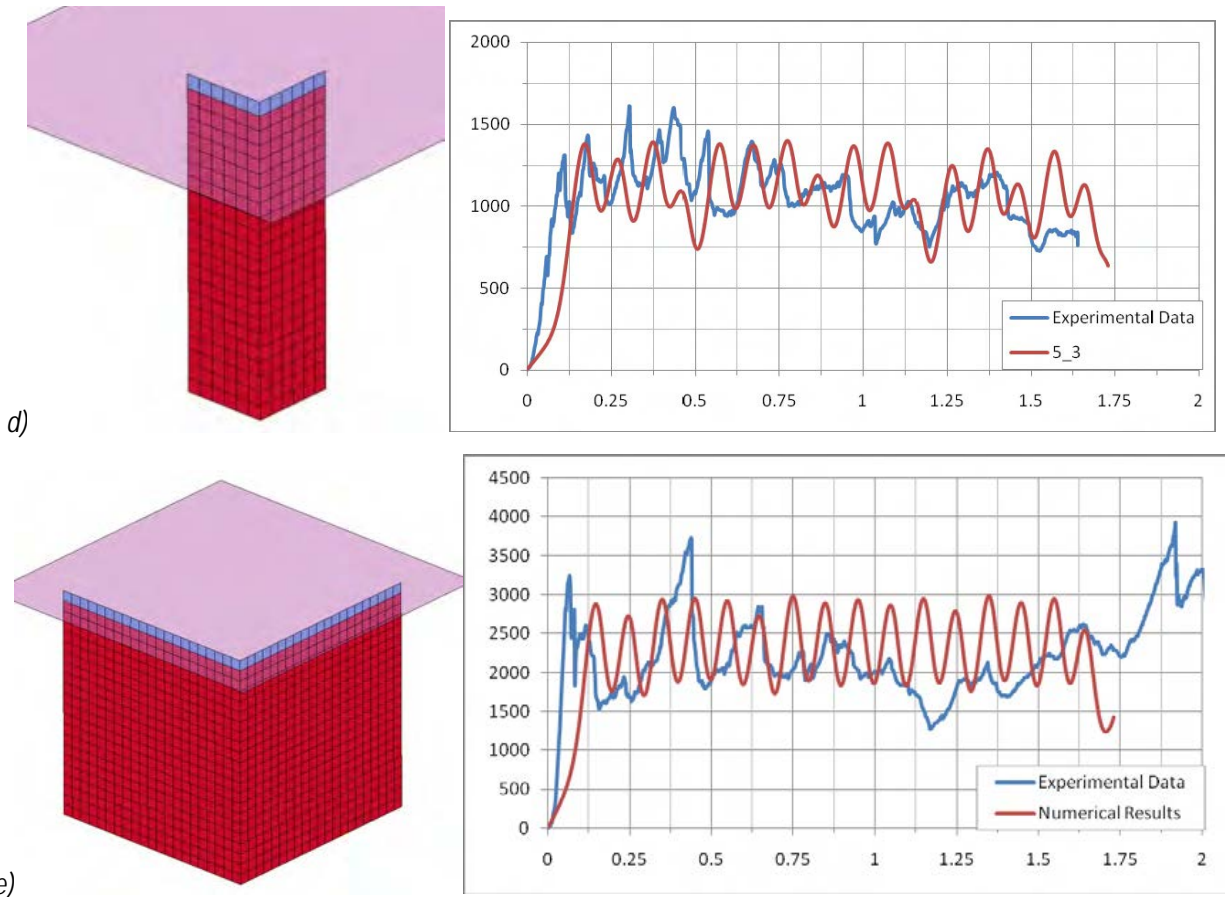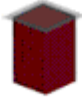
a)

b)

c)

d)

e)
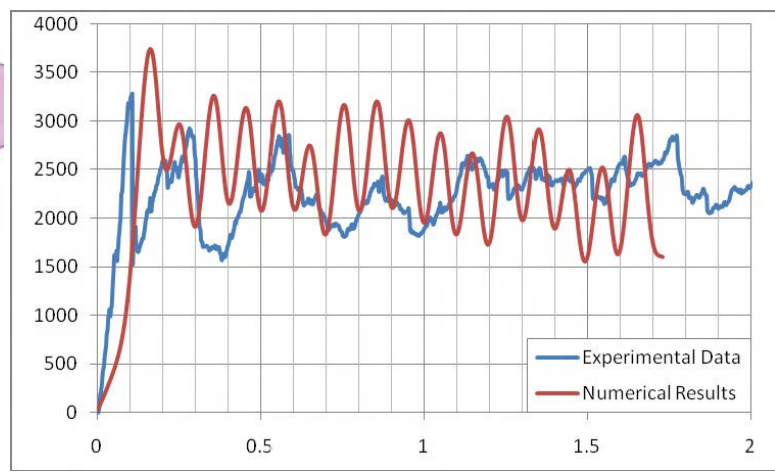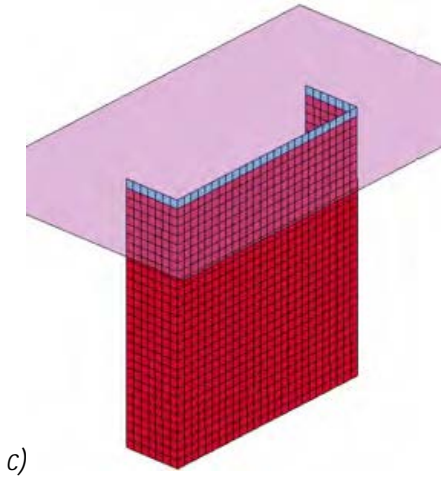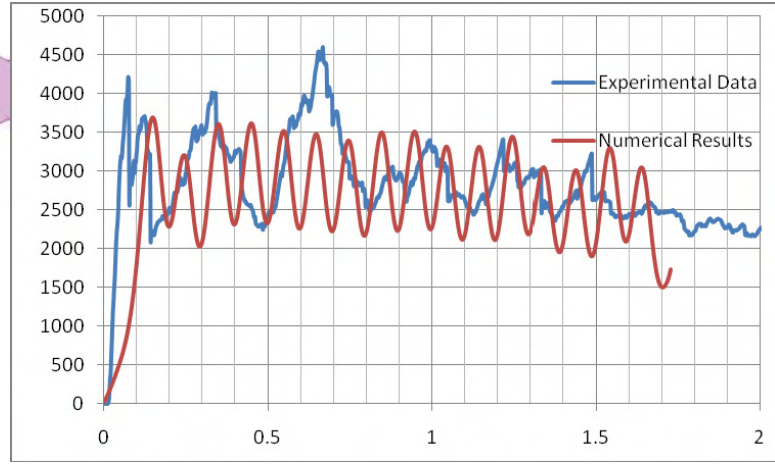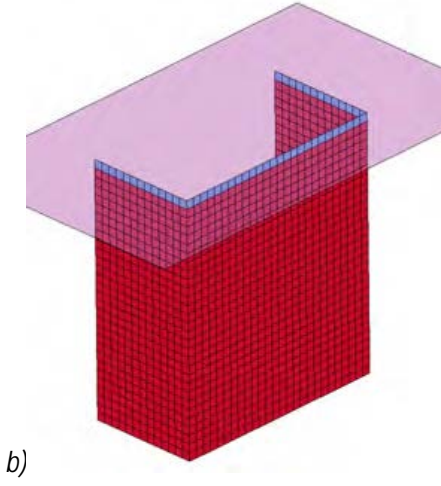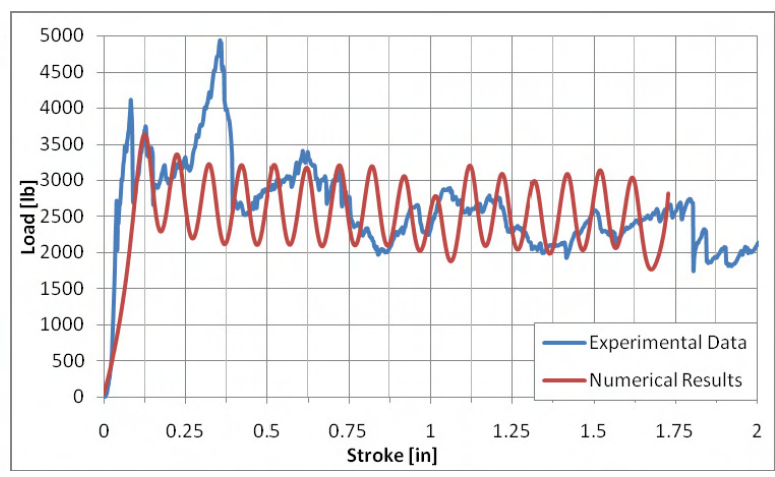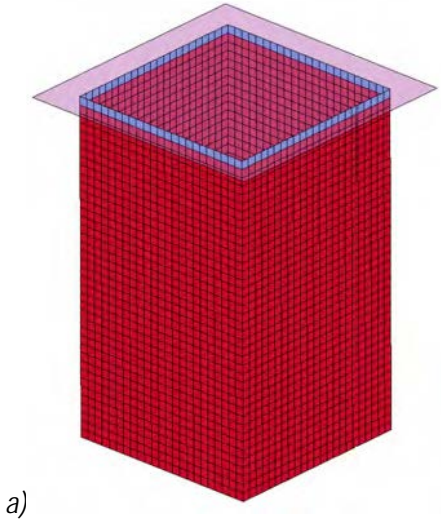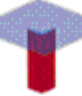
Figure 25 a-e. Model geometry and optimal Load-Displacement curve for the square tube (a), large C-Channel (b), small C-Channel (c), small corner (d), and large corner (e) specimens.

Table VIII. Dimension, SEA and SOFT parameter value for each geometry type.

Geometry type		Cross-sec A [in^2]	W [in]	Cross-sec L [in]	H [in]	Thickness [in]	SEA [J/g]	SOFT Calibrated
Tube		0.335156	2.3	4.6	4.1	0.07286	36.9	0.085
Large C-channel		0.378872	2.6	5.2	3.1	0.07286	42.7	0.23
Small C-channel		0.29144	2.6	4.0	3.1	0.07286	36.9	0.22
Small corner		0.087432	0.6	1.2	2.2	0.07286	62.30	0.33
Large Corner		0.306012	2.1	4.2	2.2	0.07286	31.6	0.21

Figure 26. Linear relation between the SEA and SOFT parameter.

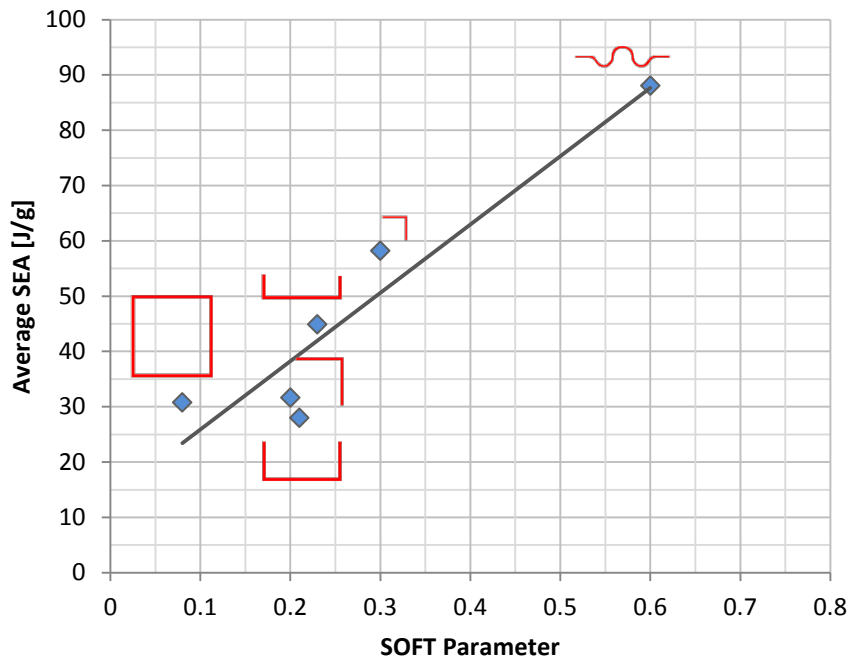It appears therefore that the SOFT parameter has therefore a physical meaning, associated to the degree of curvature of the cross-section, and hence its ability to perform well under axial crushing conditions. The more contoured (i.e. not flat) the section, the more stable it will be. Contoured sections tend to suppress the formation of delaminations, and is key in preventing the formation of large intact fronds. This in turn facilitates crushing and tearing over splaying/ frond formation, and hence it yields higher amounts of SEA. The smaller the delamination, the small the damage zone ahead of the crash front, and hence the higher the amount of pristine material available to dissipate energy. In LS-DYNA MAT54 this is captured by having higher values of SOFT parameters for more contoured geometries. The SOFT parameter can be physically related to the degree of damage that propagates ahead of the crashfront, and that affects the residual strength of the material that is about to become the crashfront.

Predictive Modeling of an Energy-Absorbing Sandwich Structural Concept using the BBA

The complexity associated with crash modeling of composite structures has been of the most limiting factors in the widespread introduction of composites in the mainstream automotive industry [11]. It is then proposed by the authors to utilize the BBA, widely used in the aerospace community but often not utilized in the automotive industry, for the certification by analysis supported by test evidence of an energy-absorbing structural concept for a high performance vehicle, representative of a doorsill structural concept.

The doorsill structural concept is a sandwich fabricated of composite facesheets, honeycomb core and film adhesive. The structure is 37.8 in. (960 mm) long, 7.87 in. (200 mm) wide, and 7.87 in. (200 mm) thick. In the vehicle, the structure spans from A-pillar to B-pillar, and is oriented sideways, with one facesheet oriented outward, and the other oriented toward the passenger compartment. Representative to the "Oblique side pole impact test" required by the Federal Motor Vehicle Safety Standard (FMVSS) No. 214 [28], a rigid pole impacts the outer

facesheet, penetrates into the core for up to 80% of its depth, but does not intrude into the inner facesheet. Although the part has a complex geometry, tapering both in width and height from the front of the vehicle to the back, it can be idealized as a flat beam resting against a rigid, flat surface being intruded mid-span by the rigid pole. The details for materials and fabrications are presented in [29]. Several tests, of varying complexity and cost, are performed along the allowable, element and sub-component levels of the BBA pyramid. At the coupon level, material properties for the carbon fiber fabric material used for the facesheets are derived by means of tensile, compressive and shear tests. Tests were carried about according to the respective ASTM standards. With these properties, it is possible to generate all input data necessary for generating the MAT 54 material card used to simulate the facesheets.

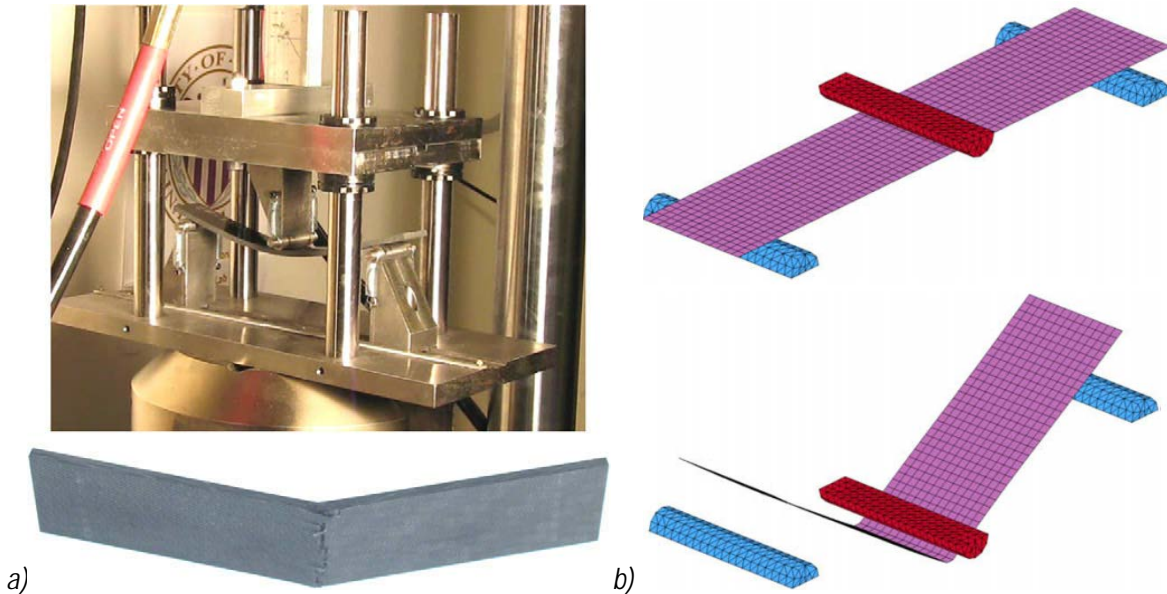*a)*   *b)*

Figure 27 a-b. Three-point bend flexure element-level test: specimen in the test fixture being loaded and after failure (a). Three-point simulation of the facesheets, at the beginning and the end of the loading (b).

Element-level tests are performed on specimens that are already specific to the structural configuration of the energy absorber concept. Moreover, the purpose of these tests is not to generate input material properties for the material models, but to generate specific load–displacement curves to be used to calibrate the material models. For the facesheets, a three-point bend flexure test is performed according to ASTM standard D790. The specimen being loaded in the dedicated test fixture is shown in Figure 27a, and has dimensions 6.5 in. long (165.1 mm) x 1.0 in. wide (25.4 mm) x 0.157 in. thick (4 mm). The corresponding finite element simulation is shown in Figure 27b. The value of flexural strength obtained is not used as input for the MAT 54 card. However, the load–displacement curve obtained during this test is used for calibration of the MAT 54 material card, since the strain-to-failure in the model needs to be modified by trial and error in order to achieve good correlation between simulation and experiment. The tensile stress–strain curve for the facesheet material, as measured from the experiment and in its final modified version for the simulation is shown in Figure 28. For the honeycomb, a stabilized core crush test at quasi-static loading rate of 1.0 in./min (25.4 mm/min) is performed according to ASTM standard D7336 to generate the load–displacement curve. The specimen has dimensions 4.72 in. long (120 mm) x 4.72 in. wide (120 mm) x 7.87 in. thick (200 mm). The test curve is used as input in the MAT 126 material model. It will be seen that, unlike for MAT 54, this empirical material model relies purely on load–displacement data generated experimentally. The model does not have the power to produce a predicted load–displacement curve based on the material properties of the aluminum core.
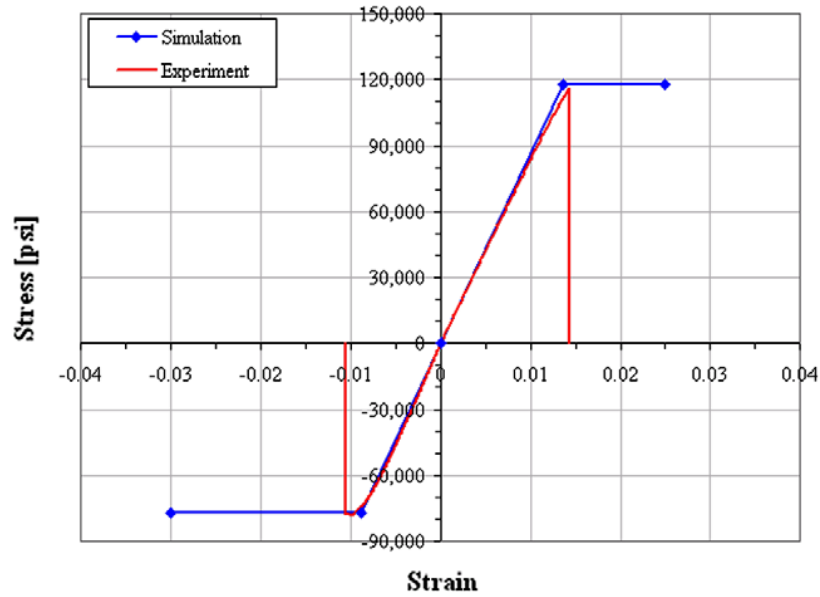
Figure 28. Tensile stress–strain curve for the facesheet material, as measured from the experiment and in its final modified version for the simulation.

The progression of the crush is shown in Figure 29a, together with the final shape after full compaction. The respective core crush simulation is shown in Figure 29b.

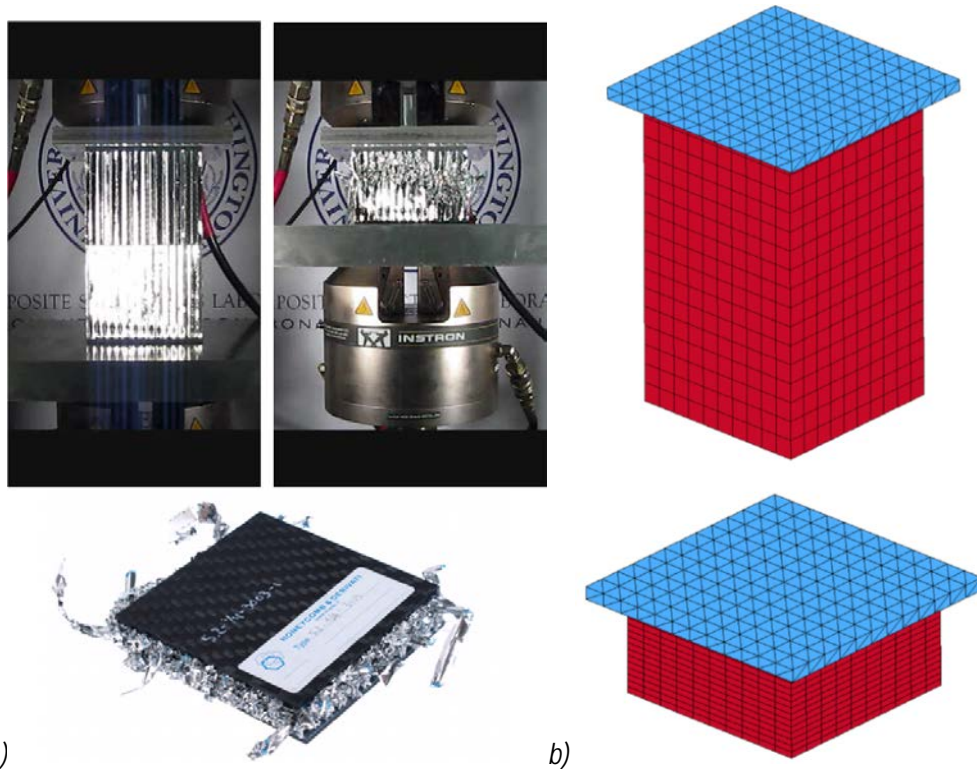a)   b)

Figure 29 a-b. Core crush element-level test, during the test and at full compaction (a). Core crush simulation, at the beginning and the end of the loading (b).

For the adhesive, single-lap shear tests are performed at a quasi-static loading rate

according to ASTM standard D1002, using two identical composite factsheets. Each of the two specimens has dimensions are 6.0 in. long (203.2 mm) x 0.5 in wide (12.7 mm) x 0.157 in. thick (4.0 mm). Figure 30a and b shows the specimen before and after failure, indicating that successful cohesive failure is achieved, and the respective single-lap shear test simulation. The adhesive is modeled using a tiebreak contact algorithm, where the peel and shear adhesive strength are the ones experimentally derived.
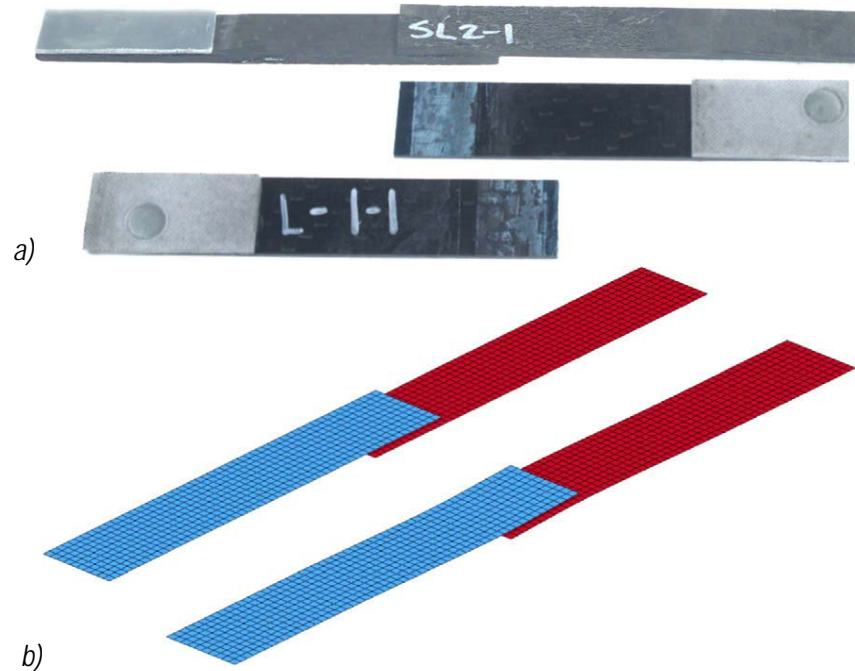

Figure 30 a-b. Single-lap shear element-level test for the adhesive, before and after failure (a). Single-lap shear simulation of the adhesive, at the beginning and the end of the loading (b).

A flat sandwich beam of the same size of the door sill component is manufactured and subjected to quasi-static penetration/ crushing using a steel pole identical to the one used in the full-scale crash test [29]. The beam rests on a fixed, rigid steel surface and is free to rotate. The morphology of failure for the beam is shown in two different instants during the penetration in Figure 31, while the respective finite element model is shown in Figure 32. The boundary conditions of the test configuration attempt to represent the conditions of the component in the vehicle as close as possible, with the inner facesheet constrained from deforming inward and intruding into the passenger compartment. This test is used to generate a load–displacement curve, which is used exclusively to validate the assembly-level FE model. At this level, the model needs to be fully predictive; hence it shall no longer be calibrated or "tweaked". Any subsequent modification, even if required to match experimental data, would result in the loss of ability to use the model as a predictive tool. In Figure 33 the experimental and numerical results are compared.

The results of the full-assembly experiment and simulation are considered favorable. The disciplined effort followed by the authors to perform the calibration of the various material models and contact definitions has enabled a high degree of confidence in the predictive capabilities of the model. Scaling up to the actual component level configured doorsill within the global vehicle simulation can be performed with the confidence that all fundamental aspects of the simulations are well understood. Nonetheless, this achievement comes at a high price. Dozens of tests have been performed at the coupon level, a few at the element level, and one at the sub-component level.

Figure 31. Partially crushed morphology of the assembly (top), the test was interrupted to take the picture. Final morphology of the assembly after testing (bottom).
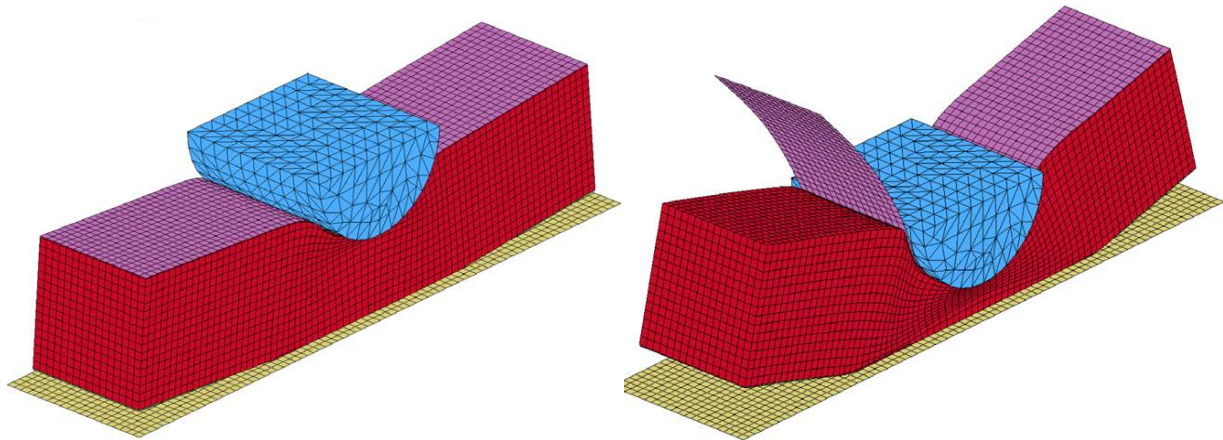

Figure 32. Subcomponent level simulation of the full-scale assembly partially penetrated (top) and at the end of the simulation (bottom).

Over a hundred simulation trials have been performed at the element level, and a dozen at the sub-component level. Parameter sensitivity studies and trial-and-error simulations have been used to find optimal values for those parameters that either could not be measured experimentally or needed to be modified from the experimental ones in order for the simulation to run successfully. For example, the load to failure of the tie-break contact used to simulate the strengths between facesheets and honeycomb were changed from those obtained experimentally on facesheet-to-facesheet joints. Although physically explainable, this change

has not been validated by element level testing. Nonetheless, the simulation runs successfully both with the nominal strength values, as well as for the reduced values. The effect on the load–displacement
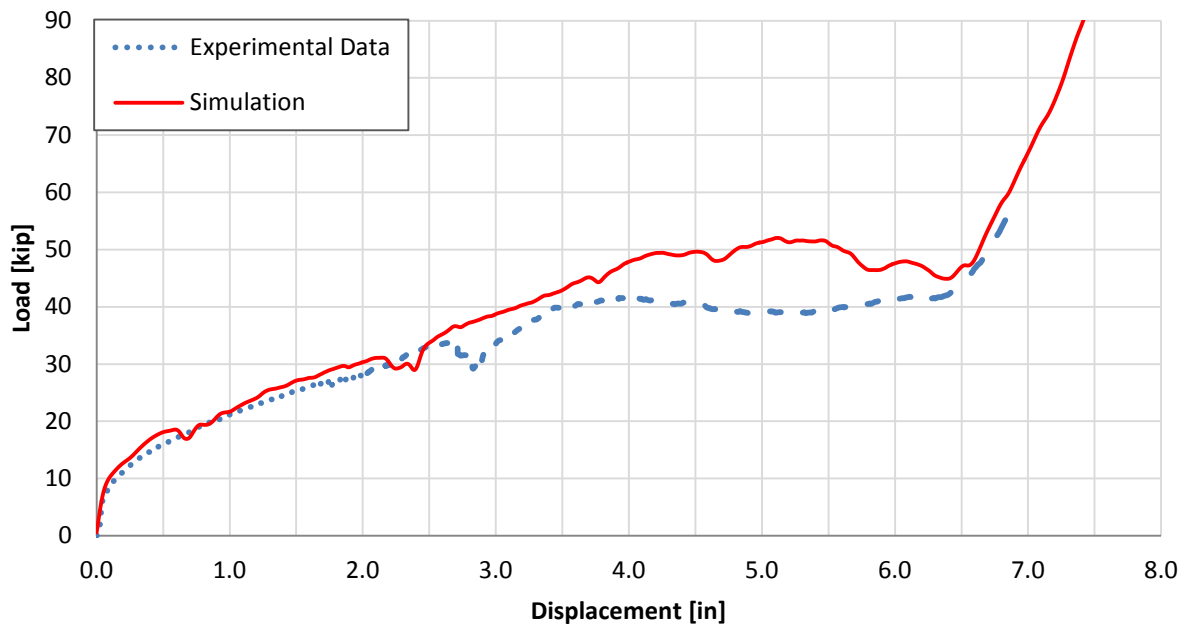

Figure 33. Comparison of experimental and simulated assembly level test, of which one uses the measured adhesive strengths, the other the reduced set of strengths.

Summary and Next Steps

Starting from a baseline of a fabric prepreg square tube, a sinusoidal specimen and five additional shapes with different geometric characteristics have been successfully crushed. Laminate thickness, material system, manufacturing process, and test methodology used are kept constant throughout the study to specifically isolate the effects of cross-section geometry on the crush behavior for each specimen. Experimentally, it is found that for the material and lay-up considered, the small corner element is the most efficient in absorbing energy per unit mass compared to the other specimens with longer flanges. The more contoured the specimen (i.e. the least amount of flat segments), the higher the measured SEA. Fiber tensile fracture and tearing at the corners is responsible for the vast percentage of the energy absorbed, while frond formation and splaying of the large flat segments is responsible for a much lower percentage. In order to maximize the energy absorption it becomes fundamental to suppress delamination propagation and to minimize formation of large fronds while promoting fragmentation as failure mechanism. A systematic investigation is carried out at a single-element level to assess the merits and limits of the LS-DYNA progressive failure material model, MAT54. Numerically, it is found that the SOFT crash front parameter in LS-DYNA MAT54 is the single most influential modeling parameter, and that is capable of modifying the shape of the simulated load-displacement curve enough to perfectly match the experimental results. It is also found that the value of this parameter is not constant for the material, but needs to be varied for each specimen geometry. By trial and error, it is possible to identify a value of the SOFT parameter that can produce perfect agreement between simulated and experimental load-displacement curves. It is also found that this apparently "tweaking" parameter has in effect a deep physical interpretation. The higher the degree of curvature of the specimen, the more efficient it is in

crushing by fragmentation rather than frond formation. The formation of large intact fronds is highly inefficient from an energy absorption standpoint, and is accompanied by the formation of long delamination in the specimen ahead of the crash front itself. This mechanism in turn acts as to create an effective damage length, which is not effective in absorbing energy. The extent of this damage length is captured by the value of the SOFT parameter, which reduces the strength of the row of elements directly ahead of the crash front.

The building block approach can be used to simulate with success the problem of a deep sandwich panel being penetrated by a rigid pole. While several experiments are needed, at different levels of complexity, to generate material model input properties and to calibrate modeling parameters that cannot be measured by test, the approach enables the designer to develop accurate analytical models, thus reducing the number of tests required to be performed at the full-scale level. Commercial FE software LS-DYNA is used to successfully model all key aspects of the problem, including the composite facesheet flexural damage, honeycomb crushing, and adhesive disbonding. Analytical and experimental correlations of load–displacement curves, energy absorption, and global morphology of the failed specimen are very satisfactory. However, this kind of simulation has posed significant challenges for the analyst, who has been required to perform hundreds of runs to define, by trial-and-error, the optimal values for several modeling parameters. These calibration efforts need to be performed with systematic rigor and a constant effort to correlate them to physical quantities, in order to avoid losing all confidence in the predictive capabilities of the model. Predictive modeling increases safety, confidence in design, and is the foundation for the development of competitive technology and design.

Finally, an ongoing research effort has been undertaken by the authors in order to explain and resolve the issue of the mesh size sensitivity of MAT54 to values much smaller or greater than 0.1 inches.

References

1. Carruthers, J.J., Kettle, A.P. and Robinson, A.M., "Energy Absorption Capability and Crashworthiness of Composite Material Structures: A Review", Applied Mechanics Reviews, 51, 1998, pp. 635-649.
2. Browne, A., Johnson, N., Botkin, M., "Dynamic crush response of RTM crash boxes", ASC 24th Technical Conference, Memphis, TN, September 2008.
3. Composite Materials Handbook (CMH-17), "Crashworthiness and Energy Management", Volume 3, Chapter 13, Rev. G
4. Johnson, A., "Determination of composite energy absorption properties", Proceedings of the 50th MIL-HDBK-17 Coordination Meeting – Crashworthiness Working Group, Chicago, IL, Jul. 2006.
5. Bolukbasi, A.O., Laananen, D.H., "Energy absorption in composite stiffeners", Composites, 26/4, 1995, pp. 291-301.
6. Feraboli, P., "Development of a corrugated test specimen for composite materials energy absorption", Journal of Composite Materials – 42/3, 2008, pp. 229-256.
7. Feraboli, P., "Development of a modified flat plate test specimen and fixture for composite materials crush energy absorption", Journal of Composite Materials 43/19, 2009, pp. 1967-1990.
8. Lavoie, J.A., Morton, J., "Design and application of a quasistatic crush test fixture for investigating scale effects in energy absorbing composite plates", NASA CR 4526, July 1993.
9. Jackson, K., Morton, J., Lavoie, J., Boitnott, R., "Scaling of energy absorbing composite plates", Journal of the AHS, 39/1, 1994, pp. 17-23.
10. El-Hage, H., Mallick, P.K., Zamani, N., "A numerical study on the quasi-static axial crush characteristics of square aluminum tubes with chamfering and other triggering mechanisms", International Journal of Crashworthiness, 10:2, pp. 183-196.
11. Feraboli P, Rassaian M, Xiao X. Progress of the CMH-17 numerical round robin: year III. In: Proceedings of the 7th crashworthiness working group meeting, 54th CMH-17 coordination meeting.

Salt Lake (UT); March 2009.

12. Greve, L., Pickett, A. and Payen, F., "Experimental Testing and Phenomenological Modeling of the Fragmentation Process of Braided Carbon/Epoxy Composite Tubes Under Axial and Oblique Impact," Composites Part B: Engineering, Vol. 39, No. 7-8, pp 1221-1232, 2008.

13. Hinton, M.J., Kaddour, A.S., Soden, P.D., "A comparison of the predictive capabilities of current failure theories for composite laminates, judged against experimental evidence", Composites Science and Technology, 62/ 12-13, 2002, pp. 1725-1797.

14. Xiao, X., "Modeling Energy Absorption with a Damage Mechanics Based Composite Material Model", Journal of Composite Materials, March 2009; vol. 43/5, 2009, pp. 427-444.

15. Feraboli, P., Rassaian, M., "Proceedings of the CMH-17 (MIL-HDBK-17) Crashworthiness Working Group Numerical Round Robin", Costa Mesa, CA, July 2010.

16. Hallquist, J.O., "LS-DYNA Theoretical Manual", Livermore Software Technology Corporation, 2005.

17. Feraboli, P., "Static strength determination of laminated composite materials within the current certification methodology for aircraft structures". Journal of Aircraft, 46/4, 2009, pp. 1365-1374.

18. MIL-HDBK-17. Building block approach for composite structures, vol 3, Ref F. West Conshohocken (PA): ASTM International; 2002 [Chapter 4].

19. Tomblin, J., Sherraden, J., Seneviratne, W., Raju, K.S., "A-basis and B-basis Design Allowables for Epoxy-based prepreg Toray T700SC-12K-50C/ #2510 Plain Weave Fabric", AGATE-WP3.3-033051-131, Sept. 2002.

20. "T700SC 12K/ 2510 Plain Weave Fabric", Composite Materials Handbook (CMH-17), Volume 2, Chapter 4.2.38, Rev. G.

21. Feraboli, P., Norris, C., McLarty, D., "Design and certification of a composite thin-walled structure for energy absorption", International Journal of Vehicle Design, Vol. 44/ 3-4, 2007, pp. 15-36.

22. Hull, D., "A unified approach to progressive crushing of fiber-reinforced composite tubes", Composite Science and Technology, Vol. 40, 1991, pp. 377-421.

23. Chang, F., Chang, K., "A progressive damage model for laminated composites containing stress concentrations", Journal of Composite Materials, Vol. 21, 1987, pp. 834-855.

24. Hashin, Z., "Failure criteria for unidirectional fiber composites", Journal of Applied Mechanics, Vol. 47, 1980, pp. 329-334.

25. Bisagni, C., Di Pietro, G., Fraschini, L., Terletti, D., "Progressive crushing of fiber-reinforced composite structural components of a formula one racing car", Composite Structures, 2005, Vol. 68/4, pp. 491-503.

26. Deb, A., Lakshmanan, P., Kharat, D., Lakkad, S., "Composite versus steel rails for vehicle front impact safety", Proceedings of the IMPLAST 2010 Conference. Providence (RI); October 2010

27. Fasanella, E. L., Jackson, K.E., "Best practices for crash modeling simulation", NASA TM-2002-211944, ARL-TR-2849, October 2002.

28. FMVSS Standard No. 214. Amending side impact dynamics test adding oblique pole test, US DoT/NHTSA Final Regulatory Impact Analysis; August 2007.

29. Feraboli, P., Deleo, F., Wade, B., Rassaian, M., Higgins, M., Byar, A., Reggiani, M., Bonfatti, A., DeOto, L,. Masini, A., "Predictive modeling of an energy-absorbing sandwich structural concept using the building block approach", Composites (Part A), 41/6, 2010, pp. 774-786.